CHARACTERIZATION OF MICROSTRUCTURE, DEFECTS, AND MECHANICAL PROPERTIES OF ADDITIVE MANUFACTURED NICKEL-BASE SUPERALLOYS

by

Erica Stevens

Submitted to the Graduate Faculty of

The Swanson School of Engineering in partial fulfillment

of the requirements for the degree of

Bachelor of Philosophy

University of Pittsburgh

2015

UNIVERSITY OF PITTSBURGH

SWANSON SCHOOL OF ENGINEERING

This thesis was presented

by

Erica Stevens

It was defended on

April 7, 2015

and approved by

David Dunand, PhD, Materials Science and Engineering, Northwestern University

Ian Nettleship, PhD, Mechanical Engineering and Materials Science

Albert To, PhD, Mechanical Engineering and Materials Science

Thesis Director: Markus Chmielus, PhD, Mechanical Engineering and Materials Science

CHARACTERIZATION OF MICROSTRUCTURE, DEFECTS, AND MECHANICAL PROPERTIES OF ADDITIVE MANUFACTURED NICKEL-BASE SUPERALLOYS

Erica Stevens

University of Pittsburgh, 2015

Due to the excellent high-temperature performance of nickel-based superalloys and the need for complicated geometries and simple repairs, methods of creating nickel-based superalloy parts by additive manufacturing (AM) are currently being developed. In this study, Laser Engineered Net Shaping (LENS) is used as the AM process to create samples, and Inconel 718 is used as the nickel-based superalloy. LENS is an AM method that uses a laser to selectively melt metal powder, while introducing additional powder in order to add to the volume of the melt pool. This process is commonly used for part repair; however, the processing parameters and resulting structure and properties of the material are not yet fully understood. This study characterizes Inconel 718 samples fabricated using LENS printing using optical microscopy, energy-dispersive X-ray spectrometry, scanning electron microscopy, electron backscatter diffraction, and Vickers microhardness, and proposes explanations for the results based on the printing process.

TABLE OF CONTENTS

LIST OF TABLES

LIST OF FIGURES

PREFACE

I would like to thank the Swanson School of Engineering, Mascaro Center for Sustainable Innovation (MCSI), the Office of the Provost of the University of Pittsburgh, and Dr. Markus Chmielus for funding a portion of this work. In addition, Dr. Albert To and his group members, including Pu Zhang, are gratefully acknowledged for their collaboration and sharing of resources for the project.

I would like to thank all of my fellow group members for their support and help, and for making our work enjoyable. I would like to specifically acknowledge the work and support of Jakub Toman, Amir Mostafaei, Corrinne Charlton, Eamonn Hughes, and Meredith Meyer.

I also appreciate the tremendous love and support of my family and friends, who helped me through the mental challenges of completing a thesis. In particular, I would like to recognize the encouragement of my boyfriend, Spencer Evans, and the proofreading genius of my best friend, Chris Dumm.

Last but not least, I would like to thank my research advisor, Dr. Markus Chmielus, for being himself: for having an infectious love of knowledge and research, for believing in me even when I didn't believe in myself, for raising the bar and expecting excellent work, and for making me excited to come to work every day.

1.0 INTRODUCTION

Compared with traditional manufacturing techniques, additive manufacturing (AM) produces less waste, requires fewer production steps, and is able to produce more complicated part geometries[1,2]. These features make it a favorable technique, at least for small scale production, repairs, or complicated part geometries; however, the effects of processing parameters on the structure and properties of materials are still not well understood. Since the thermal profiles of parts produced by AM are unlike those of parts produced traditionally, their microstructures often vary radically as well. Not only do the structures of AM parts differ from those of traditionally manufactured parts, they also differ from each other based on the method used, processing parameters, and part geometries. It is therefore important that the microstructures are examined, understood, and linked to particular AM processing methods and parameters so that these variables can be adjusted in order to produce the desired microstructures and mechanical properties[3].

1.1 BACKGROUND

1.1.1 Additive manufacturing

Additive manufacturing (AM) is a method of creating an object by selectively adding material, rather than subtracting or shaping it. AM is defined by the ASTM standard F29272-12a essentially

as the joining of material in a manner prescribed by a 3D model, in order to create an object. Manufacturing is typically done using one of many layer-by-layer deposition methods, in contrast to subtractive manufacturing and formative manufacturing[4,5]. 3D printing is often used as a synonym for additive manufacturing, though it refers more specifically to methods that use a print head, nozzle, or similar printer technology[5]. This paper is concerned with layer-based methods which can be accurately referred to as 3D printing.

1.1.1.1 From model to part

In order to create an object with the desired geometry using AM, a 3D computer-aided design (CAD) model is first created and turned into an STL file, which uses a mesh of triangles to describe the surface geometry. Then, machine-specific AM software converts the STL file into a slice file; it cuts the part into layers and saves the data from each layer[6,7]. The thickness of these layers depends on factors such as the time available for fabrication, the accuracy of the fabrication method, the desired accuracy of the part and machine-specific parameters[7].

Due to the layering process, a curved or slanted surface which is intended to be smooth shows instead what is often called a "staircase effect"[7,8]. This effect is produced when slices with rectangular edges are stacked to create a curved or slanted surface; each layer and its contribution to the part are clear, and the surface is not smooth. As layer thickness diminishes, so do the discontinuities resulting from the staircase effect (Figure 1)[9].

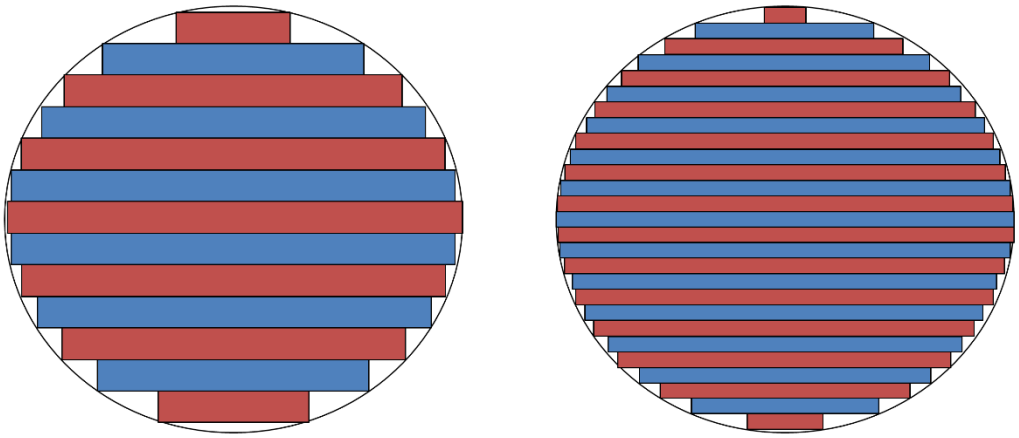

Figure 1. Staircase effect in a part with thicker layers (left) and thinner layers (right).

Once the slice file is created using the necessary layer thickness, it is sent to the 3D printer. The machine creates each layer from the bottom up, printing each new layer on top of the existing layers. Though there are many different methods that may be used to generate individual layers, the layer-by-layer process flow itself remains the same for all layer-based 3D printers[8,10].

1.1.2 LENS manufacturing

Laser engineered net shaping (LENS) is an additive manufacturing process that was developed at Sandia National Laboratories and adapted for commercialization by Optomec[4,11–13]. The LENS process takes place in a contained chamber with a constant influx of argon gas to maintain low oxygen levels. A laser beam is first focused on a small area of solid metal, creating a melt pool. Then, metal powders are added to the chamber through powder delivery nozzles (Figure 2). Some land on the melt pool, becoming a part of it and adding to its volume. The laser scans over each

layer in a manner prescribed by a CAD model, and then proceeds on to the next layer. In this way, a 3D part is created using layered 2D slices[11–14].

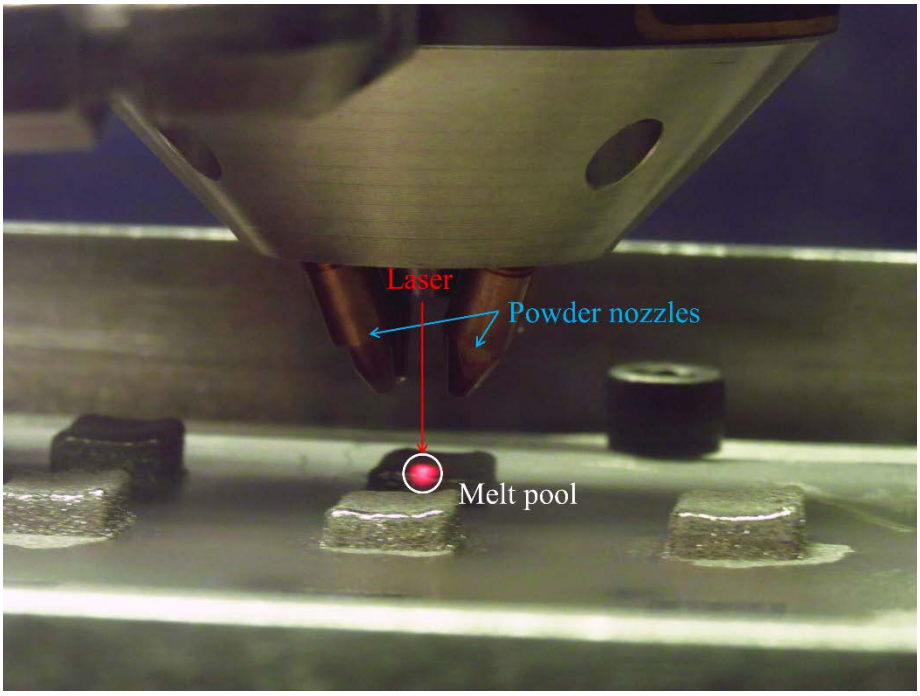

Figure 2. LENS system during printing.

The LENS process has several advantages over traditional manufacturing, and even over other 3D printing processes. LENS production creates intense thermal profiles with several cycles of quick heating and cooling, which dictates local microstructural evolution. It is also very precise and produces a very small heat-affected zone (HAZ). There are reported to be superior material properties due to the microstructure created by the thermal profile, and the precision and small HAZ are useful for selectively repairing parts that would otherwise be compromised by repair attempts[15]. In addition, the precision abilities of LENS allow for the construction of part geometries that would not be possible with other methods, such as complex cooling channels and turbine parts[12,13]. Furthermore, several powder types can be mixed in varying amounts in-situ, allowing for small-scale, local alloying[16,17].

1.1.3 Inconel 718

Inconel 718 (IN718) is a nickel-based superalloy, used primarily in the aerospace industry for high-temperature applications[18]. The structure of nickel-based superalloys is primarily that of nickel, which has an FCC crystal structure. This is beneficial for high-temperature applications because it provides a good combination of toughness and ductility. In addition, IN718 has no phase transformation from room temperature to the melting point, so the alloys maintain their properties well over a large temperature range. Though nickel may not have the very best high-temperature stability and functionality available, it is sufficient and is relatively light and inexpensive[19].

IN718 in particular is often designated as a nickel-iron superalloy due to the high amount of iron among the alloying elements. It is an alloy that is commonly wrought, and therefore is polycrystalline[20]. There are several main phases found in IN718: γ, γ', γ'', and carbides and borides. γ is the nickel-rich FCC matrix phase. γ' and γ'' are coherent with the matrix phase, and γ'' is preferred over γ' in nickel-iron superalloys such as IN718[19–21]. γ'' is an ordered BCT phase that (in IN718) is composed approximately of Ni_3Nb and appears disc-shaped within the microstructure. Though preferred, γ'' is much more difficult to observe in the microstructure, due to the fact that it is nano-sized[19,20,22].

IN718 is often manufactured using powder metallurgy (PM) methods because of its use in products with complicated geometries, especially turbine parts. Therefore, in addition to repairing turbine blades made out of IN718, LENS processing would be a useful tool for fabricating IN718 parts. It has the ability to build complicated parts precisely without a die and with little post-processing, which greatly reduces the manufacturing cost[19].

1.1.4 Thermal profile and microstructure of LENS-fabricated materials

LENS fabrication produces a unique thermal profile due to the focused laser scanning across the surface of the material. Any given area of material will experience thermal cycling: hottest when in the region of interest is inside the melt pool, cooling as the laser moves away, and heating up again (albeit with a smaller temperature gradient) when the next layer is built on top of it (Figure 3)[23].

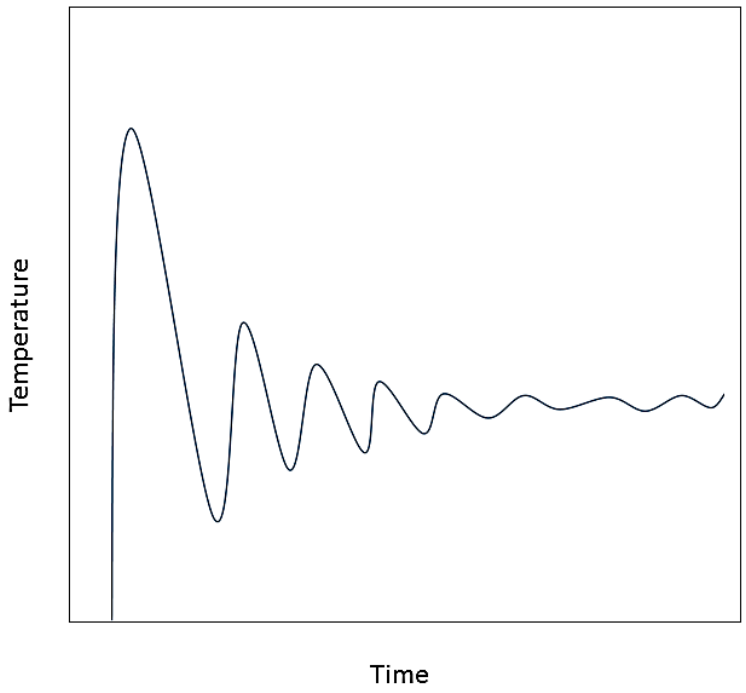

Figure 3. Thermal cycles within LENS-fabricated samples, based on computational data plot from Manvatkar et al[11]. Time and temperature for cycles will depend on printing process parameters.

This cycling continues with subsequent layers, with a general decreasing trend, producing a columnar and dendritic microstructure[11,18,24]. Also known as cells, these columnar features exhibit micro-segregation; the concentration of various elements differs from the inside of the

feature to the outside[11,25]. Micro-segregation occurs because diffusion cannot occur fast enough to homogenize the material before it solidifies[26].

1.1.5 Structure-property relationship

The microstructures of materials directly affect their mechanical properties. It has been reported that the properties of LENS-fabricated materials are generally comparable or superior to those produced by traditional manufacturing[13,25,27–29]. The favorable properties result from the fine microstructure created during rapid solidification. However, since the thermal profile of each section of the part is not identical (e.g. the higher the layer, the lower the amount of thermal cycles), the mechanical properties will vary throughout the part. As the part builds higher, it is unable to lose heat as quickly to the substrate, the cooling rate decreases, and the cell spacing and grain size increase accordingly. Larger cell spacing has been found to correspond to a decrease in hardness[11,30].

1.1.6 Scanning electron microscopy

The scanning electron microscope (SEM) uses a beam of electrons directed at a specimen to obtain a surface image or to compositional information[31]. It is beneficial to use an SEM when a greater depth of field or a higher magnification than is possible with optical microscopy is required. Often SEM is preferred over transmission electron microscopy due to the simpler sample preparation. As its name suggests, the scanning electron microscope creates an image by scanning in consecutive lines called raster. A slower scanning speed allows for a higher resolution image to be obtained. Three signals that can be detected using an SEM are secondary electrons, X-rays, and

backscattered electrons. Secondary electrons are used to create a secondary electron image, which is used to examine topography. X-rays are used in energy-dispersive X-ray spectroscopy (EDS), which is also explained below. Backscattered electrons have many uses, one being to create a backscatter electron composition (BEC) image, where contrast arises from difference in atomic weights (heavier elements appear brighter, corresponding to a greater number of backscattered electrons). Backscattered electrons are also used in electron backscatter diffraction (EBSD), which is explained below[31].

1.1.6.1 Energy-dispersive X-ray spectrometry

Energy-dispersive X-ray spectrometry (EDS) is a compositional analysis tool used within the SEM. As the electron beam interacts with the sample, one of the resulting signals is characteristic X-rays, which are emitted when an excited outer shell electron jumps to a vacancy in the inner shell[31]. EDS uses these characteristic X-rays to determine which elements are present and in what amounts.

A common EDS detector consists of a cooled semiconductor behind a thin beryllium window, surrounded with a gold film. It is known that the number of electron-hole pairs created by a given incoming X-ray photon is proportional to that photon's energy. When a voltage is applied to the detector, current flows as X-rays are detected. The magnitude of the current is indicative of the energy of the incoming X-ray, and can therefore be used to identify the element that produced the X-ray[31,32].

Each X-ray photon creates a pulse of current, which is analyzed and registered in the correct energy range (channel). The result of this analysis is a histogram which increases in resolution with an increased amount of channels within the same energy range. Identification of elements is done either automatically by the computer or by selecting known elements, which are then marked

on the histogram by a vertical line at the appropriate energy[31]. Sometimes however, when elements are very close together in energy, it can be difficult to distinguish between their peaks on the histogram.

1.1.6.2 Electron backscatter diffraction

Electron backscatter diffraction (EBSD) is a diffraction method which uses backscattered electrons to determine crystallographic information. The backscattered electron coefficient (η) is the amount of backscattered electrons emitted per incident electron. This gives rise to an effect called electron channeling, since the backscattered electron coefficient is affected by the position of a given crystal in relation to the incident beam. The contrast that is caused by the varying amount of escaping backscattered electrons is therefore called channeling contrast, and it is typically very weak. A good detector and ideal sample preparation and microscope conditions are needed to obtain a diffraction pattern[31,33].

As with X-ray diffraction, Bragg's Law governs the patterns that are seen due to constructive and destructive interference in EBSD[31]. Bragg's Law states that constructive interference occurs when $n\lambda = 2d \cdot \sin\theta$, where n is an integer, λ is the incident wavelength with an incident angle of θ, and d is the interplanar spacing within the crystal[34]. Each set of planes which satisfies the Bragg condition diffracts in Kossel cones. These cones of diffracted electrons radiate out at a wide angle and therefore are essentially two parallel straight lines when they hit the phosphor screen detector, which then emits light. This resulting set of two lines is called a Kikuchi band. A full EBSD pattern contains many bands, which reflect the crystal's symmetry, as well as the spacing of atoms in the plane, and the angles between planes[33].

Due to the fact that EBSD patterns are collected from only the surface of the sample (~50 nm), sample preparation and surface quality is extremely important. Any contamination, residue,

or slight deformation will decrease the quality of the scan. In order to obtain excellent EBSD patterns, one or several of the following techniques is recommended (depending on the material): vibratory polishing, electropolishing, chemical etching, or ion etching[33].

1.2 EXPERIMENT

Two sets of IN718 samples were prepared. The first set of four samples varied the laser travel speed and software layer height. A second set of samples was prepared by varying the linear energy using a change in the scanning speed with a constant laser power.

1.2.1 Manufacturing details

Both sets of samples were made using an Optomec LENS 450 system. Each sample was a prism of approximately 10 mm x 10 mm x 3-5 mm and was printed in 10 layers. Each layer was printed by first building the *contour*, the outside edge. After this square frame was created, the middle was filled in by the laser scanning back and forth in parallel lines to create what is referred to as the *hatching*. These lines were made at 0˚ in the first layer, 45˚ in the second layer, 90˚ in the third, 135˚ in the fourth, and so on. The hatching overlapped the contour slightly, meaning that the contour got overbuilt and became higher than the hatching of the same layer. A schematic of the build process and terminology can be seen in Figure 4.

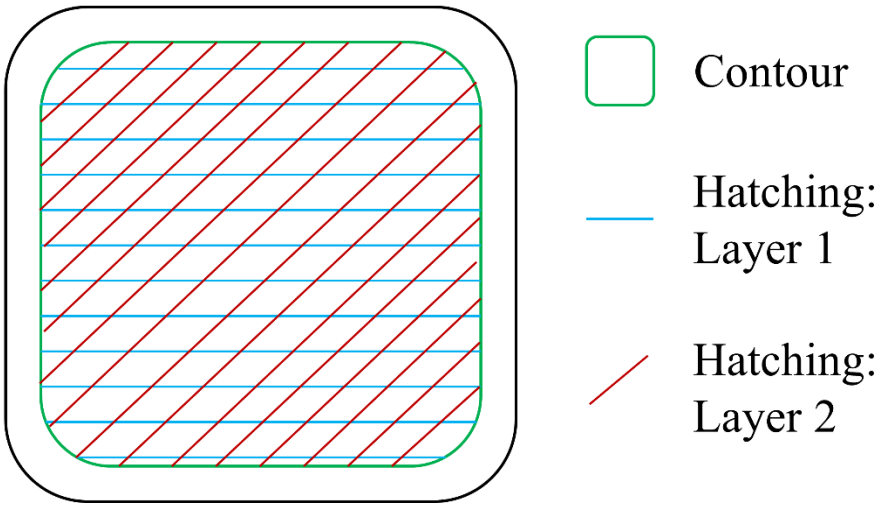

Figure 4. Schematic of build process and terminology (top view of a sample).

A schematic of the build path for each layer is given in Figure 5. For the purposes of describing the details of the manufacturing process, the side of the stage and substrate that was oriented closest to the viewing window will be referred to as the front, the side furthest from the window as the back, the side towards the right when facing the viewing window as the right, and the remaining side as the left.

First, the system zeroed in the back right corner of the sample, without starting the laser. Then, the laser was oriented over the start point of the contour and was turned on automatically. Though the contour start points were consistent between samples in corresponding layers, there was no pattern to their location between layers of the same sample. In one continuous bead of material, the outline, or contour, of the material was built. The build direction of the contour alternated between clockwise and counterclockwise. After the contour was complete, the system turned off the laser, positioned itself over the start point of the hatching, and turned the laser back on again. As with the contour starting points, the starting points of the hatching were consistent, though with no pattern between layers. After each individual hatching line was complete, the laser

turned off, the system moved over slightly to the beginning of the next hatching line, and the laser turned on again. At the end of the hatching, the laser turned off, returned to the zero point in the back right corner, and began the next layer in the same way.

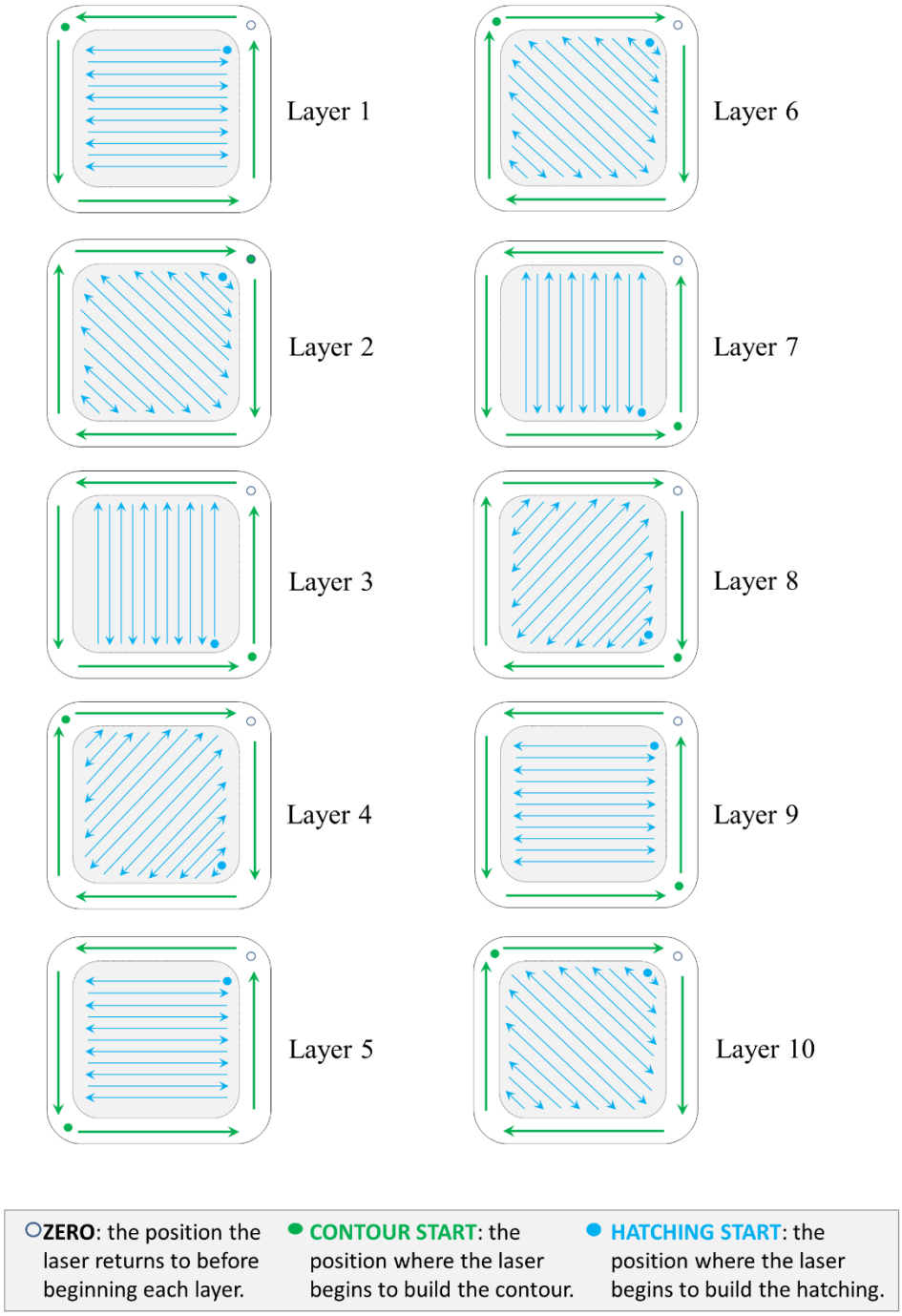

Figure 5. Schematic of the build path for each layer of the sample prisms.

Note: number of hatching lines is not to scale, and contour was built as one continuous bead.

1.2.2 Sample details

The first set of samples consisted of four samples, labelled A, B, C, and D, and were made on an IN718 substrate with IN718 plasma rotating electrode process (PREP) powder of 44-150 µm diameter. A laser power of 250 W and a hatch distance of 0.254 mm were used. Additional details on the build parameters can be found in Table 1.

Table 1. Build parameters for LENS-printed IN718 samples A, B, C, and D.

		Laser travel speed	
		2 mm/s	2.27 mm/s
Layer height in software	0.254 mm	A	B
	0.203 mm	C	D

The second set of samples consisted of two samples, labelled 1 and 2. These were also made on an IN718 substrate with IN718 PREP powder of 44-150 µm diameter. Laser power and hatch distance remained the same as for the first set of samples (250 W and 0.254 mm, respectively). Layer height in the software was maintained at 0.254 mm, and only the laser travel speed was changed. This created a varying linear energy, which is equal to the laser power divided by the laser travel speed. For sample 1, the travel speed was 5 mm/s, resulting in a 50 J/mm linear energy. For sample 2, the travel speed was 3.33 mm/s, resulting in a 75 J/mm linear energy. Samples A and B had linear energies of 125 J/mm and 110 J/mm, respectively. These parameters are shown in Figure 6.

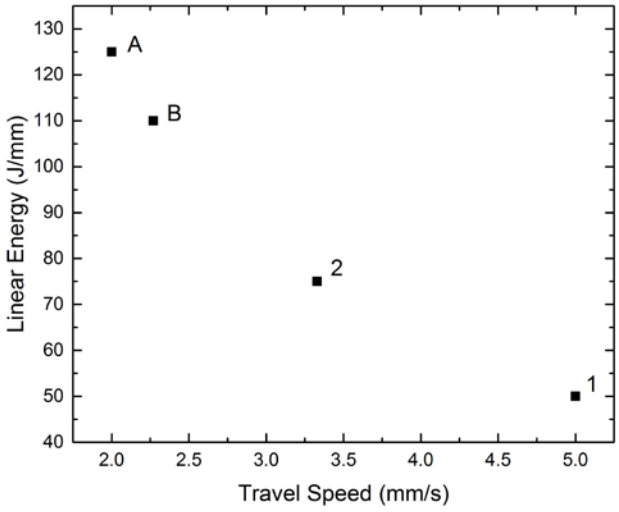

Figure 6. Printing parameters for samples A, B, 2, and 1 in terms of linear energy based on varying travel speeds.

1.2.3 Imaging and sample preparation

Each sample was imaged in the as-printed condition using a Keyence digital optical microscope (DOM) with a dark field Z20 lens and a multi-diffused adapter or focal distance adapter at varying magnifications. After the initial structure was documented, the samples were separated by using a metallographic saw to cut the substrate around each prism. This resulted in separate samples: small pieces of substrate, each topped with one of the prisms. Each of these pieces was then hot compression mounted, ground, and polished. Phenolic resin was used as the mounting material for the first set of samples, and graphite powder was used for the second set of samples due to the benefits of having conductive mounting during electron microscopy. The progression of SiC paper used for grinding was 400-, 600-, 800-, and 1200-grit. Final polishing was accomplished using a 0.5 μm Al_2O_3 suspension followed by a 0.05 μm Al_2O_3 suspension. After polishing, the samples

were examined and imaged again with the DOM in bright field and dark field, with both Z20 and Z100 lenses.

Samples A, B, 1, and 2 were cut in half using a metallographic saw in order to access the cross-section. The cross-sections were polished in the same way as outlined above. The cross-section of sample A was swabbed for 10 seconds with Waterless Kalling's Etchant to reveal features of the microstructure (Number 94 in ASTM E407[35]).

In addition to an optical microscope, each polished sample was examined using a JEOL JSM6610 scanning electron microscope (SEM). Images were taken using both secondary electrons and backscatter electrons with a compositional contrast. The SEM was also used to collect compositional data using energy-dispersive X-ray spectrometry (EDS) and grain distribution data using electron backscatter diffraction (EBSD). EDS was done on the JEOL JSM6610 (Figure 7) in the form of point scans and line scans.

Figure 7. JEOL JSM6610 scanning electron microscope, used for imaging and energy-dispersive X-ray spectroscopy.

The point scans were done for 30 seconds in each of the distinct regions in a backscatter image (e.g. dark, light, dim, and bright). Line scans were done for approximately 200 seconds across regions of distinct contrast in a compositional backscatter image. EBSD was done at 50x magnification, an 18 mm working distance, an accelerating voltage of 25 keV, and a spot size of 5 on a Philips XL 30 (Figure 8).

Figure 8. Philips XL 30 scanning electron microscope, used for electron backscatter diffraction.

On the faces of samples A, B, C, and D, EBSD was performed in regions that spanned both hatching and contour, with a square grid scan of 1500 µm x 1500 µm and a step size of 0.5 µm. EBSD was also done on the cross-section of sample 1, from the substrate up through almost the top layer of the sample. EBSD of the cross-section of sample 1 was done in two separate scans due to time and area restrictions when at 50x. The first scan was 900 µm x 1800 µm with a 0.3 µm step size and began in the substrate and extended approximately 1.28 mm into the sample. The second

scan was 900 μm x 1800 μm with a 0.3 μm step size and was taken overlapping the first area, and extended an additional 0.6 mm towards the top of the sample. In total, the sample area scanned was close to 1.8 mm, which is near the total sample height of 2.1 mm. The interface with the mounting material was unable to be scanned due to its interference with Kikuchi pattern formation.

1.2.4 Microhardness

Mechanical properties were assessed with a Leco hardness tester via Vickers microhardness measurements with a load of 300 or 500 gf and a dwell time of 10 s. Two grids of indents were made on each sample face, placed to sample the contour as well as the hatching. More densely-packed indents were made on the top and middle slices of sample A in order to obtain a more comprehensive mapping of hardness values.

Hardness maps were created for the top and center slices of sample A, as well as for the cross-section of sample 1. Indents for mapping were made with 500 gf and a 10 s dwell time, and were placed 200 μm apart (center-to-center). The grids parallel to the substrate, which were created on the top and center slices, were approximately rectangular, spanning one quarter of the sample face area (Figure 9).

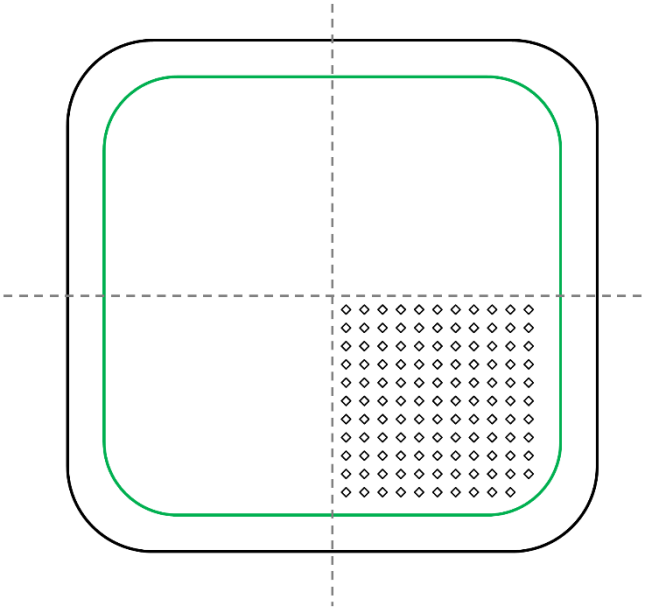

Figure 9. Representation of hardness mapping location based on symmetry of the sample face. Number of indents and indent spacings are not to scale.

The grid perpendicular to the substrate, on the cross-section, were made by following the edge of the sample as closely as possible with rows and columns. These indents spanned approximately one third of the sample cross-section.

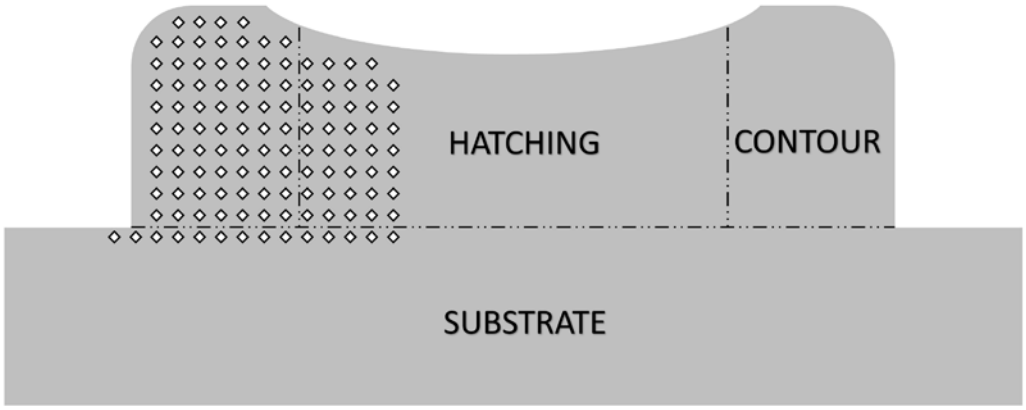

Figure 10. Schematic of hardness mapping area on cross-section of sample 1. Number of indents and indent spacings are not to scale.

Indent size was measured using two different microscopes: the Olympus BX-60M optical and the Keyence digital optical microscope. The Olympus requires that the user indicate the diagonals of the indent, from which it automatically calculates the hardness using parameters that the user specifies. Based on microscope availability, the Keyence was also used to make indent measurements. The Keyence does not calculate hardness automatically, so each diagonal was measured and the averages for each indent were used in the Vickers microhardness formula ($HV = 1854.4P/d^2$) to calculate hardness, where P represents the applied load in gf and d represents the average diagonal length in μm[36,37].

2.0 RESULTS AND DISCUSSION

The results obtained included optical microscopy images, SEM images, EDS/EBSD data, and Vickers microhardness data.

2.1 OBSERVATION OF DOTS WITH MICROSCOPY AND EDS

2.1.1 Dot distribution

Figure 11 shows the top view of one of the IN718 samples in the as-printed, polished, and re-polished condition.

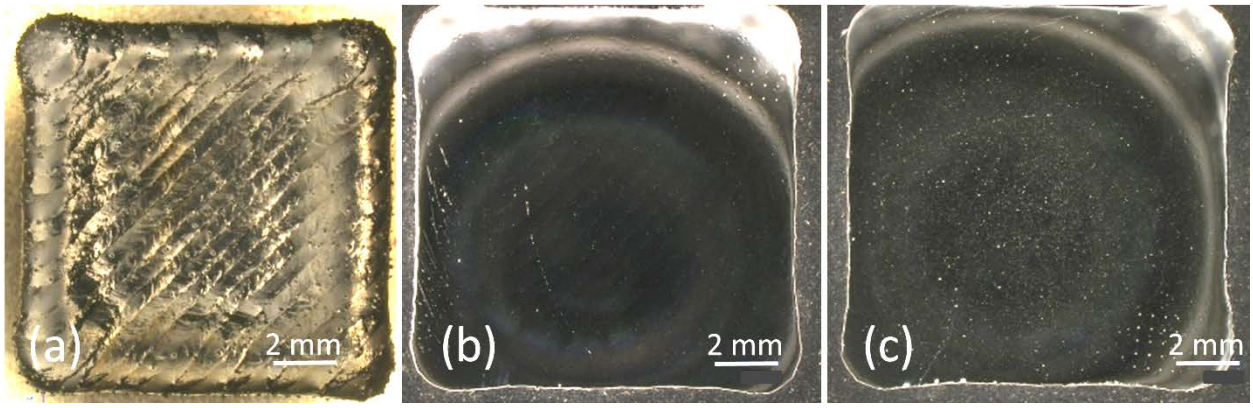

Figure 11. Top view of IN718 sample in the as-printed (left), polished (center), and re-polished (right) conditions.

There were two types of dots visible: large (20-30 μm) and small (<10 μm). The distribution of the large dots was not affected by location in the sample. The distribution of the

small dots, however, were dependent on the location in the sample. In the intralayer region, the dot distribution in the hatching followed the scan direction of the laser; in the interlayer region, the dots were more densely packed and randomly distributed. In addition, the dots in the contour region were consistently densely packed and randomly distributed (Figure 12).

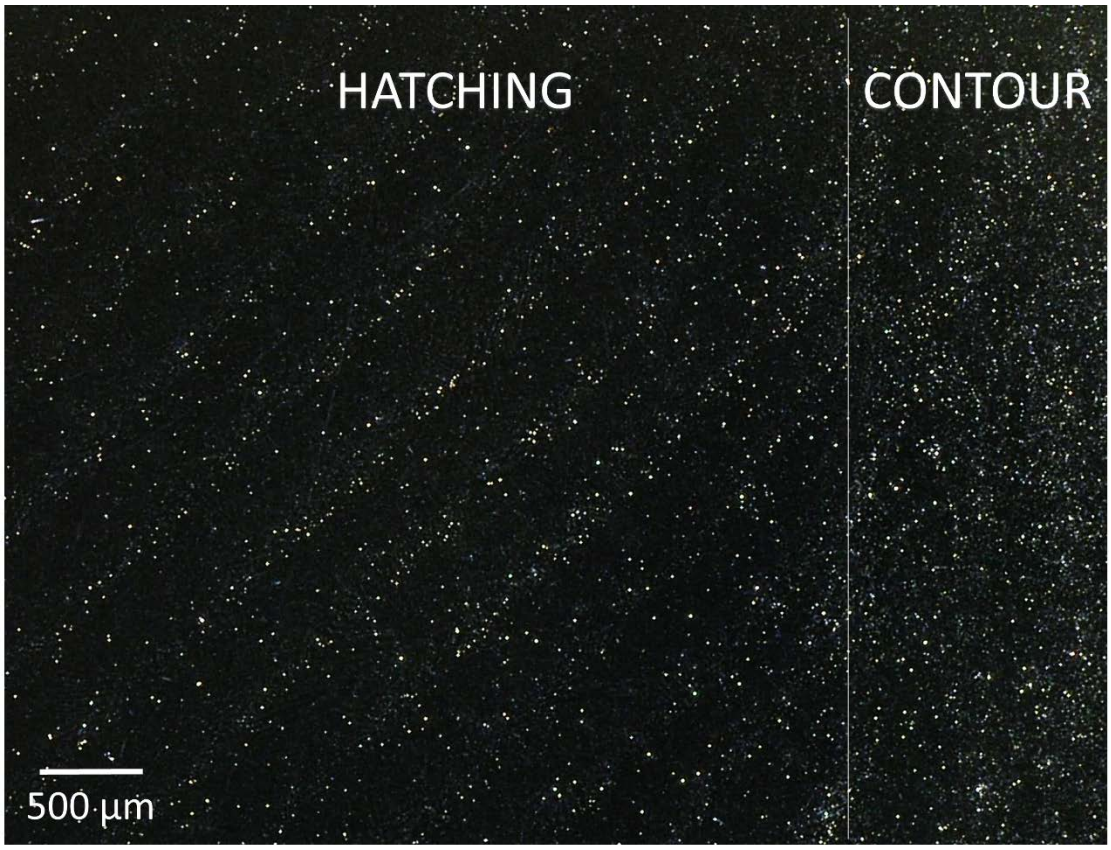

Figure 12. Optical image at 50x of difference between hatching and contour dot distribution.

The dots were seen in the SEM image in Figure 13 as black spots.

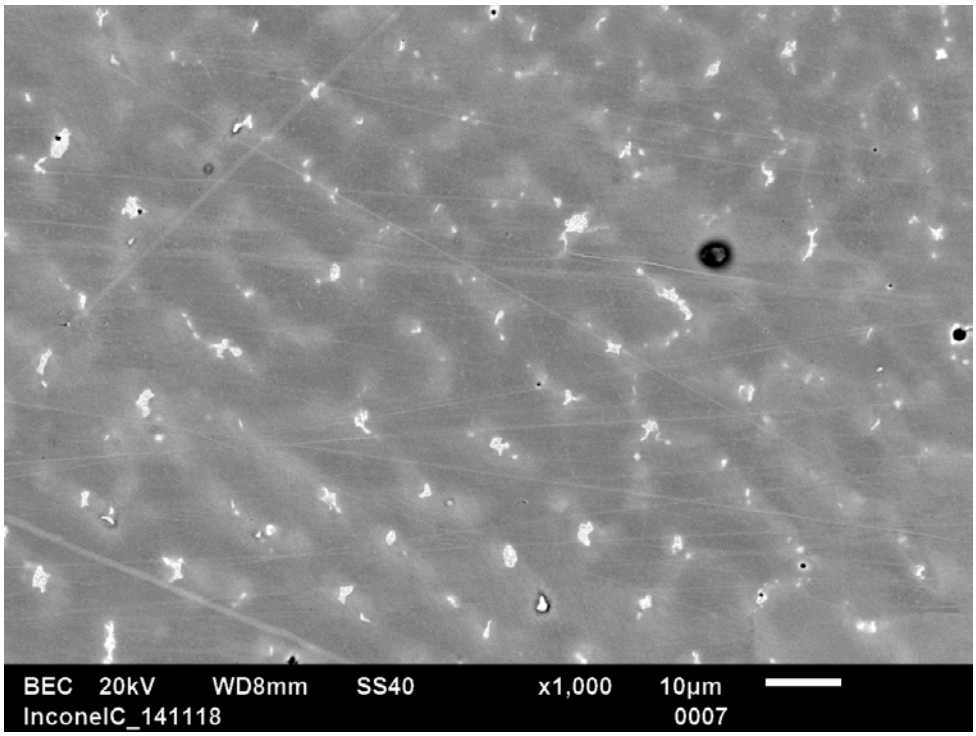

Figure 13. SEM micrograph. The black spots are the same features that appear as small bright dots in the dark field DOM image.

2.1.2 Compositional changes

Chemical composition of the dark spots was identified with EDS. Examples of spectra are given in Table 2 and compared to the expected nominal composition of IN718. As compared to the expected compositions of 0 wt.-% O and 0.5 wt.-% Al, the spots showed an increase to between 9 and 19 wt.-% O and between 1 and 5 wt.-% Al.

Table 2. EDS data for black spots, which contained more Al and O than the nominal composition (wt.-%) of IN718.

	O	Al	Ti	Cr	Fe	Ni	Nb
Spot 1	18.32	4.04	1.22	15.25	13.47	38.80	8.90

Spot 2	9.24	1.12	1.50	16.06	14.31	46.04	11.74
Spot 3	14.20	4.26	0.93	17.52	14.83	43.12	5.14
Nominal	0	0.5	0.9	19	18.5	52.5	5.1

2.1.3 Identification of dots as pores

As there are numerous phases and the possibility for inclusions within the sample, the dots were not immediately identified as pores, though they appeared as such based on the reflection of light in DOM. To confirm that the dots were pores, sonication of the initial samples after polishing was performed for only a short amount of time so that results from EDS could be examined for trapped polishing slurry. The dots showed elevated amounts of Al and O compared to the nominal composition, though the other elements in IN718 were still detectable. This information led to the conclusion that each dot was a hole, or pore, and that the interaction area of the electrons in EDS allowed the elements within the bulk IN718 material to be seen. Within the pore was remnants of polishing slurry consisting of Al_2O_3, explaining the presence of anomalous levels of Al and O.

2.1.4 Pore distribution changes

When the sample was first polished, the face was a part of the top layer deposited. After being ground and polished again, enough material was removed to expose the interface between the top layer and the one directly beneath it. This can be determined from the view of the cross-section of sample A (Figure 14), which was polished to a plane that was still within the tenth layer. In Figure

14, the top face is clearly still within the top layer, but could feasibly be polished down enough to expose the interface.

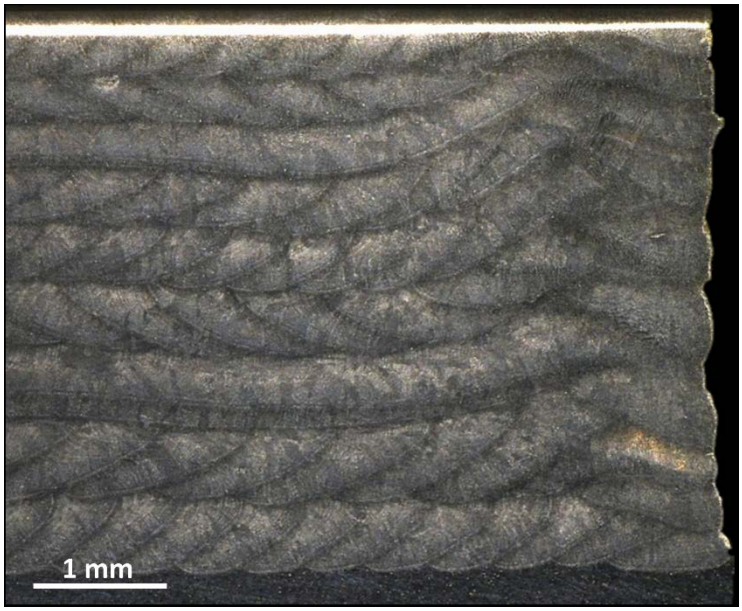

Figure 14. Part of the cross-section of sample A, where etching revealed melt pool interfaces and distinguished layers.

The scanning lines that are seen in Figure 11 were a result of the edges of melt pools, which can also be identified in Figure 14, the cross-section. The edges of the melt pools have an increased number of pores. In the top view and in the middle of a layer, these edges and their contained pores trace out the scan direction, though they do not exactly reflect the laser's path since the scan lines overlap each other. When the sample was polished to a depth which exposed an intralayer surface, the bottom of the upper melt pools met with the top of the lower melt pools, and caused a much denser and more random distribution of pores.

The difference between the distribution in the contour and the hatching can be explained in a similar way. Since the contour was built first in every layer and then the hatching was built with some overlap, there is more re-melting and more interaction between edges of melt pools in the

contour than in the hatching. Therefore, there is expected to be a denser and more random distribution of pores in the contour throughout the height of the sample.

The large pores were 20-30 µm and their distribution was not affected by location in the sample. It is possible that these pores are caused by hollow powder particles with trapped gas that would remain trapped in the sample without heat treatment for densification. Since the small pores were less than 10 µm and their distribution depended on location in the sample, it is more likely that they are a product of the process than the powder.

2.2 ELEMENTAL DISTRIBUTION

2.2.1 EDS results from sample faces

In all samples, the contour could be distinguished from the hatching through careful, unaided visual observation. The interface between the two could also be seen in a backscatter electron composition (BEC) image (Figure 15). In this image, the angled, finger-like lines from the bottom left corner are the end of the hatching, and the rest of the image is the contour. Figure 15 also shows one of the curved interfaces in this same region at a higher magnification to clarify the cause of the contrast. In a BEC image, heavier elements appear brighter than lighter elements.

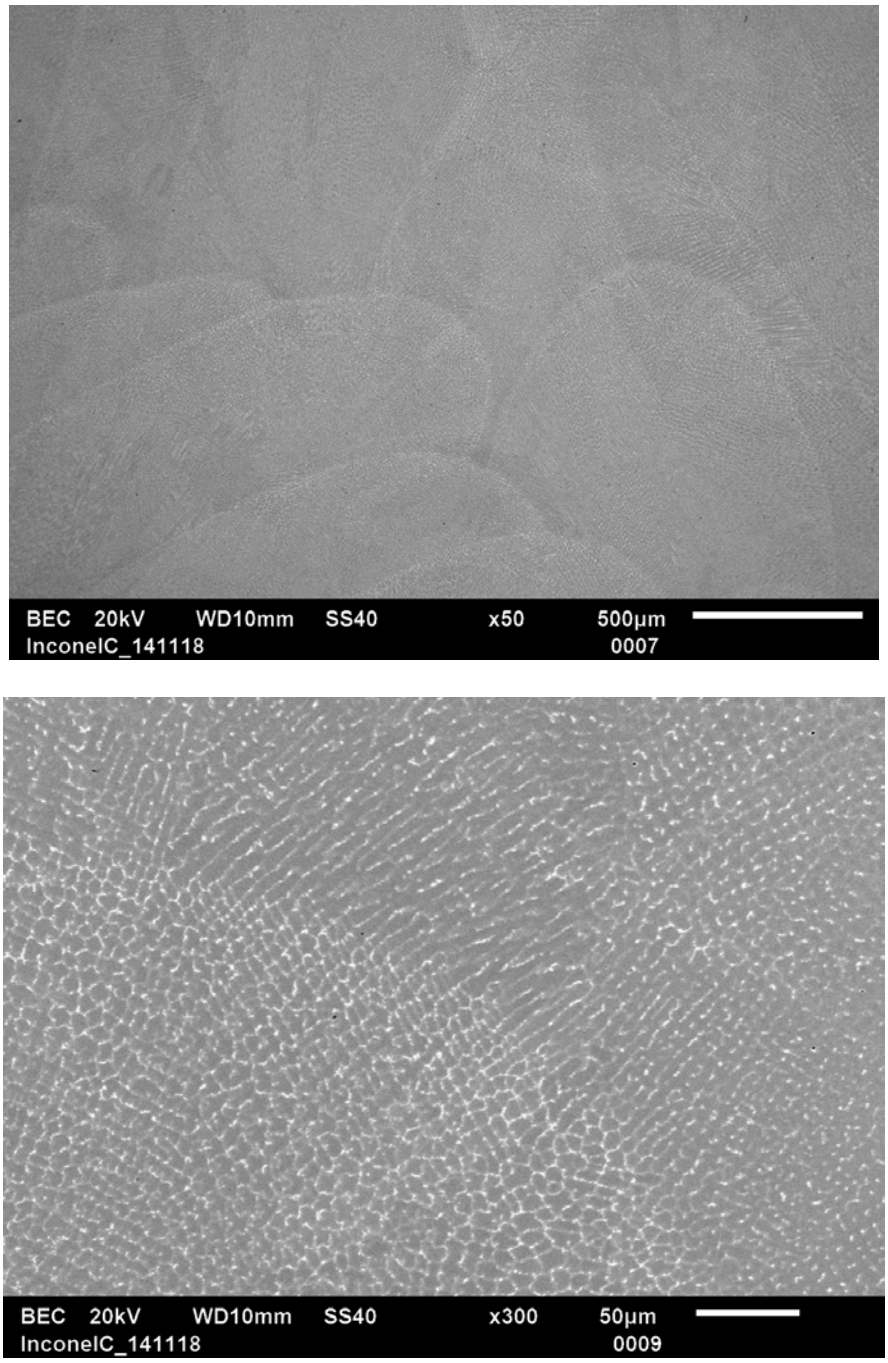

Figure 15. Backscatter electron composition image of the interface between the hatching and the contour at 50x (above) and 330x (below).

BEC images also showed the dendritic microstructure (Figure 16). There were central areas of dim gray running through the sample and branching off along the length of each area. In between

the branches were regions of light color, and interspersed at the edges of these were small, very bright regions. The regions of distinct brightness were analyzed using EDS.

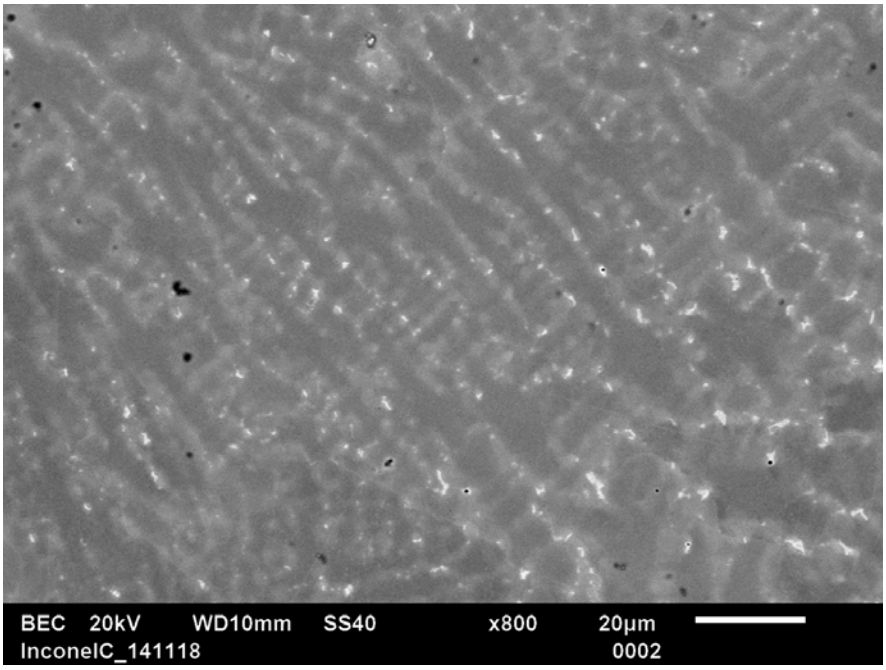

Figure 16. Backscatter electron composition image of a region of the hatching in sample C, exhibiting a dendritic microstructure.

EDS analysis showed an increase in Fe in the dim regions, an increase in Fe and Nb in the light regions, and an increase in Mo and Nb in the bright regions. It was assumed that limited amounts of O in all samples were a result of contamination and not relevant compositional changes. Within the dim region, the only significantly increased value was that of Fe. There was approximately 5.5-7.5% more Fe than in the nominal composition. Ni and Nb noticeably decreased to accommodate this increase. Overall, the light regions showed an increase of about 1.5-5% in Fe and 1-2% in Nb over the nominal. It should be noted that the anomalous value of 26.68% Nb for sample D is likely an error due to the machine not recognizing the peak for Mo, which overlaps with the Nb peak during analysis. The bright regions showed approximately 14-18% more Nb than the nominal composition, which is reported to contain about 5.5% Nb.

Table 3. Summary of EDS compositional analysis, separated to show dim, light, and bright regions in the compositional backscatter image on the face of each sample.

Dim								
Sample	O	Al	Ti	Cr	Fe	Ni	Nb	Mo
A	0.93	0.50	0.73	19.54	18.64	52.48	3.45	3.73
B	0.92	0.53	0.93	20.38	20.07	51.81	2.59	2.77
C	1.83	0.64	0.55	19.91	20.28	51.81	2.13	2.84
D	2.05	0.00	0.88	21.50	20.78	54.78	0.00	0.00
Nominal	0	0.8	1.15	21	13.17	55	5.5	3.3

Light								
Sample	O	Al	Ti	Cr	Fe	Ni	Nb	Mo
A	1.50	0.28	1.40	17.87	17.55	51.22	6.82	3.36
B	1.01	0.58	1.14	18.68	16.91	50.19	7.64	3.85
C	1.23	0.47	1.01	19.17	18.22	49.97	6.45	3.49
D	0.00	0.00	2.11	15.51	14.65	41.05	26.68	0.00
Nominal	0	0.8	1.15	21	13.17	55	5.5	3.3

Bright								
Sample	O	Al	Ti	Cr	Fe	Ni	Nb	Mo
A	0.27	0.35	1.40	14.26	13.50	45.32	19.60	5.31
B	1.99	0.32	1.58	14.39	13.65	41.21	21.33	5.53
C	1.65	0.25	1.70	14.48	13.09	42.52	22.92	3.39
D	0.00	0.00	1.06	16.27	14.55	44.16	23.97	0.00
Nominal	0	0.8	1.15	21	13.17	55	5.5	3.3

2.2.2 Discussion of elemental distribution

Through the use of BEC imaging, the hatching and contour could be distinguished. Therefore, a distinct segregation of elements must be present to create the contrast necessary for BEC images. For the interference between the hatching and contour, Figure 15 shows a certain macro-contrast: overall it shows regions of darkness and highlights, which together contribute to the distinction of the two major areas. When the large areas are examined more closely however (Figure 16), a

micro-contrast within the macro-contrast can be seen. This micro-contrast defines the dendritic microstructure which is expected from LENS, as a rapid solidification process.

Since elemental analysis was done on highly magnified regions only, and the micro-contrast affects the macro-contrast, the results from the micro-contrast analysis will be presented first and then extended to explain the macro-contrast.

2.2.2.1 Micro-contrast analysis

The dendrites in the microstructure had a dim core, which contained more Fe and less Nb and Mo than the nominal composition. Around this core was a light region, which had decreased Fe and Nb. Within this light region were bright spots that were rich in Nb and Mo. This distribution of elements suggests that the non-equilibrium rapid solidification that occurs during the LENS process carried the heavier elements of Nb and Mo with the solid-liquid interface. Therefore, when the final liquid cooled, it was saturated with Nb and Mo. These regions are likely precursors to the γ'' phase, which consists of Ni_3Nb, and is the strengthening phase in IN718. When the γ'' phase forms, it creates the regions that are bright and are significantly richer in Nb. Though the γ'' phase is nano-sized, a conglomeration of particles could still appear as the bright region seen in BEC imaging. This explanation is supported by the work of Tian et al[38].

2.2.2.2 Macro-contrast analysis

The results from analyzing the micro-contrast (or micro-segregation) can be used to also examine the macro-contrast (or macro-segregation). Each of the hatching lines is outlined by a thin line of light material. Based on the above analysis, it can be concluded that this area has an increase in Nb and Mo. Therefore, as the melt pool as a whole cooled, more Mo and Nb were swept to the edges and solidified there. When the next line was created, it re-melted one side of the previous

line a nd re-distributed t he e lements, pus hing t hem t o t he edges of i ts own m elt pool . T his anisotropic compositional distribution continued throughout each layer of hatching.

2.3 GRAIN SIZE AND DISTRIBUTION

EBSD was used to determine grain size and distribution. The scanned area on the faces spanned part of the hatching and part of the contour to detect any differences in grains between the two. The scanned area on the cross-section spanned part of the substrate and the bottom layers of the sample.

2.3.1 EBSD of sample faces

The results of the EBSD scans on the faces of samples A, B, C, and D are shown in Figure 17.

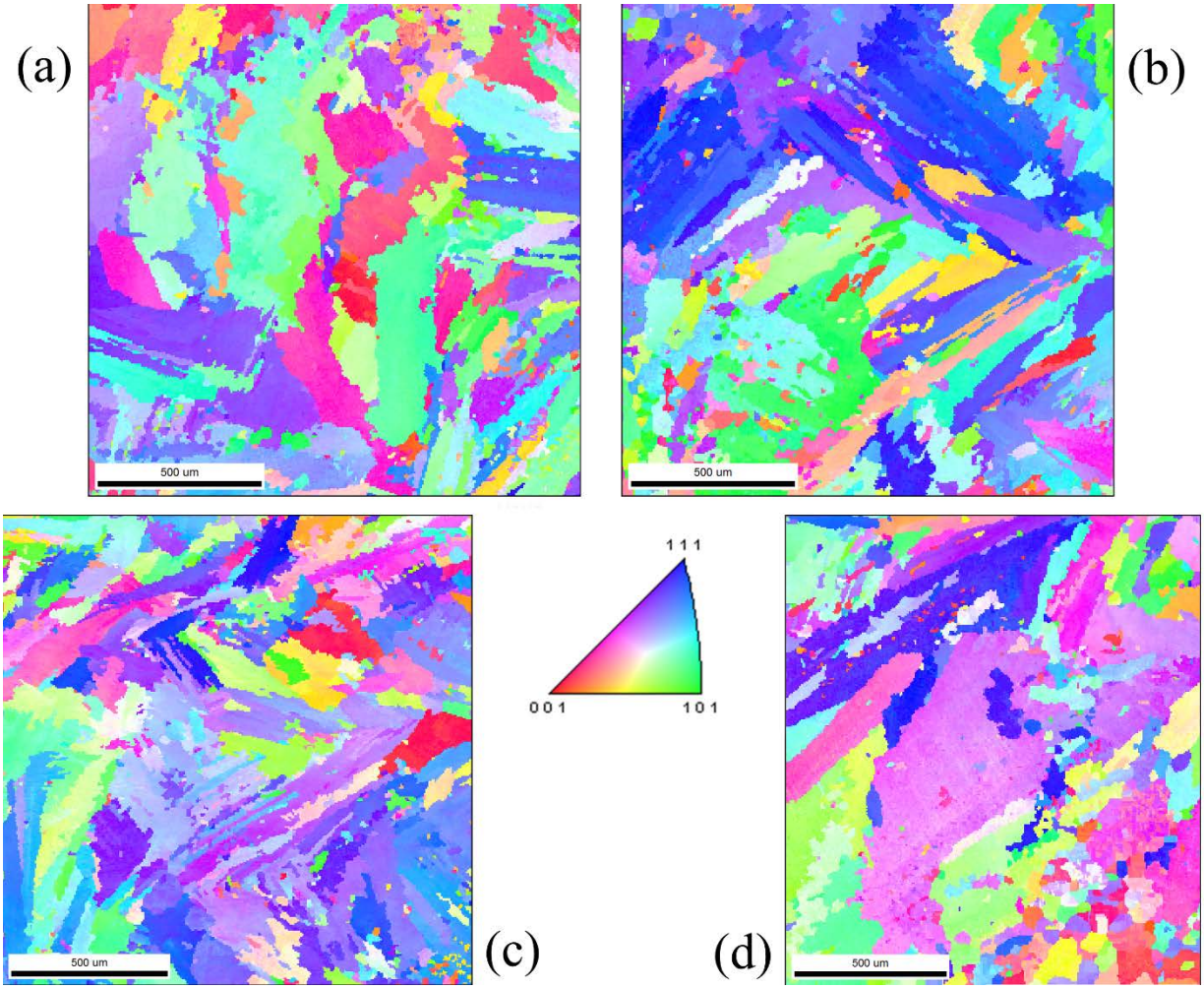

Figure 17. EBSD inverse pole figures for sample A (a), sample B (b), sample C (c), and sample D (d), with accompanying color key for out-of-plane orientation.

Each sample showed elongated, directional grains that spanned a range of orientations and sizes. In sample A, 8% of the scanned grains had an area of less than 1000 μm^2, 13% had an area 1000-5000 μm^2, 30% had an area 5000-20000 μm^2, 33% had an area 20000-100000 μm^2, and 17%

had an area greater than 100000 μm^2. With the same categories for grain sizes, the distribution for sample B was 10%, 15%, 21%, 41%, and 13%; sample C was 18%, 13%, 16%, 26%, and 28%; sample D was 7%, 17%, 18%, 20%, and 31% (Figure 18).

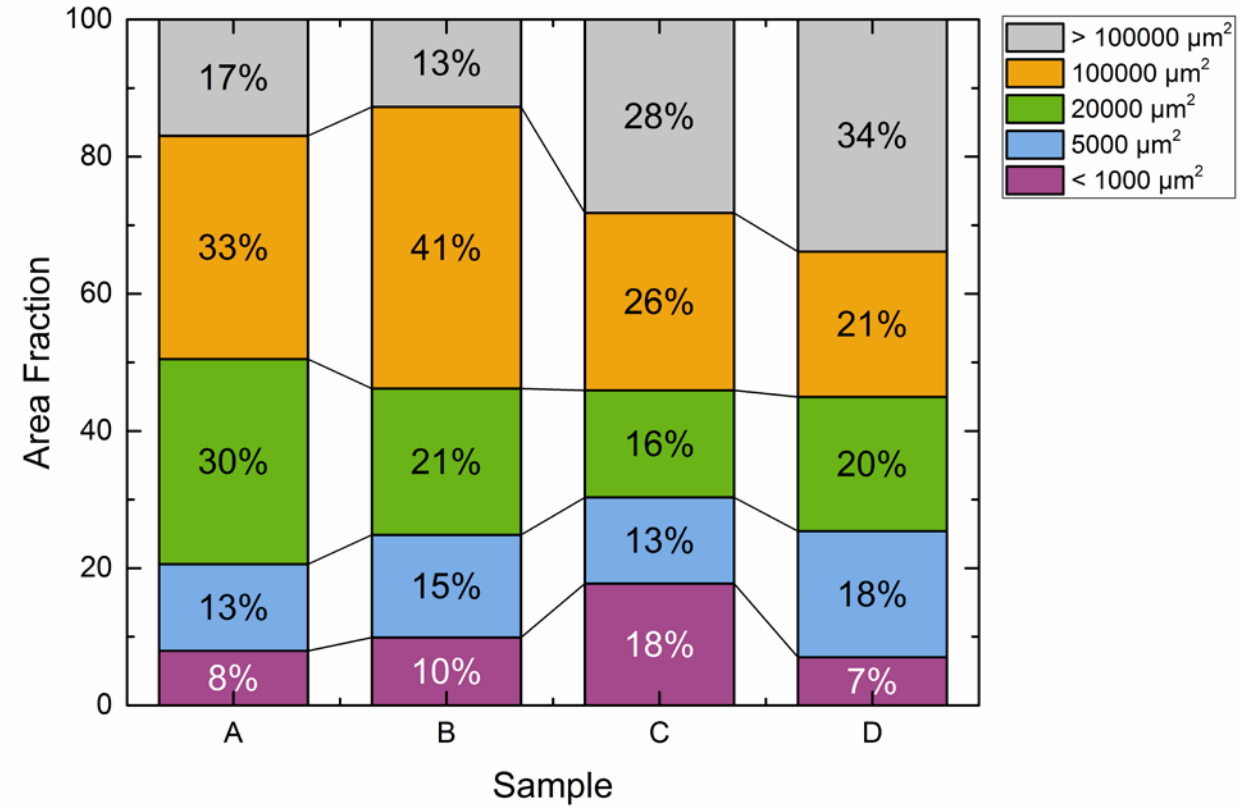

Figure 18. Grain size distribution based on EBSD data.

2.3.2 EBSD of sample cross-section

EBSD scans of the cross-section spanned much of the sample in an area where the contour and hatching interact. Figure 19 shows the result of the scans, with a schematic indicating the approximate area they were taken from.

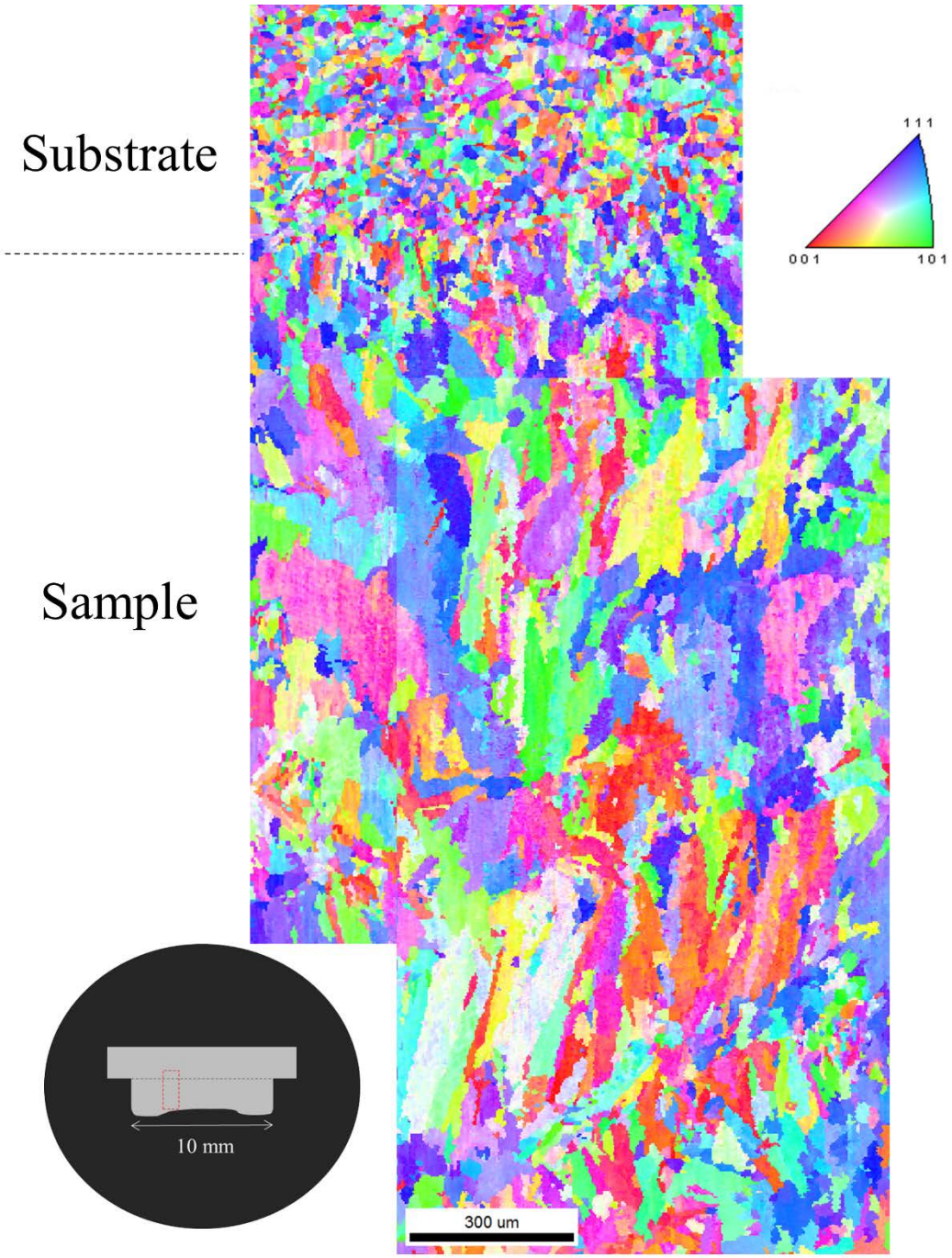

Figure 19. EBSD image of sample 1a, from the substrate into the sample.

The top part of the scan had small, mostly equiaxed grains, with no preferred orientations. Moving into the sample, the microstructure was still fairly fine-grained and the grains began to

elongate slightly along a direction perpendicular to the substrate. Going still further towards the top of the sample, the grains became coarse and elongation increased. Figure 20 shows the grain size distribution of the second scan only, since the data for the grain sizes within the sample from the first scan was skewed due to the data for the grain size within the substrate. Within the sample, there were 10% of grains less than 500 μm^2, 15% of grains between 500 and 1000 μm^2, 37% between 1000 and 5000 μm^2, 17% between 5000 and 10000 μm^2, and 21% between 10000 and 35000 μm^2.

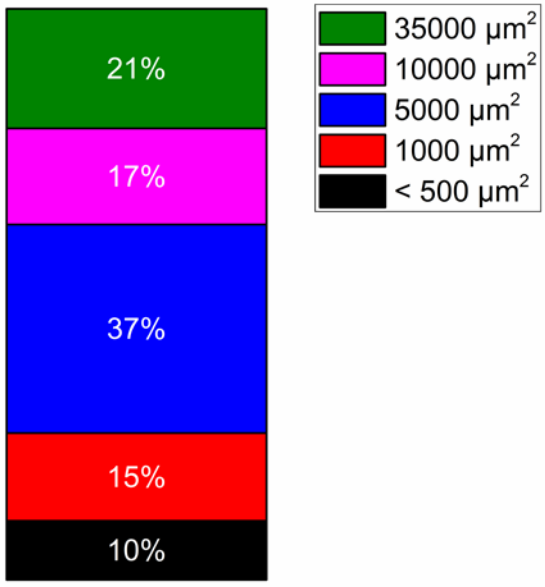

Figure 20. Grain size distribution (area fraction) from the second scan of the cross-section of sample 1.

These grains were not as large as the grains on the faces of the samples, but are still considered to be mostly in the range of somewhat coarse to coarse. The finer grains that did exist were not all clustered, but rather are spread out throughout the scan area amongst the larger grains. There was a small area of clustered smaller grains near the top of the sample, in the hatching.

2.3.3 Discussion of EBSD on sample faces

Based on visual inspection of EBSD results, there was only a potential correlation between the approximate contour and hatching lines and grain orientation in sample B. There was a seemingly uniform distribution of the types and sizes of grains in the data for samples A, C, and D that did not correspond to the estimated directions and locations of the contour and hatching. Figure 21 shows the scans from Figure 17, with the approximate hatching-contour interface and scan directions indicated.

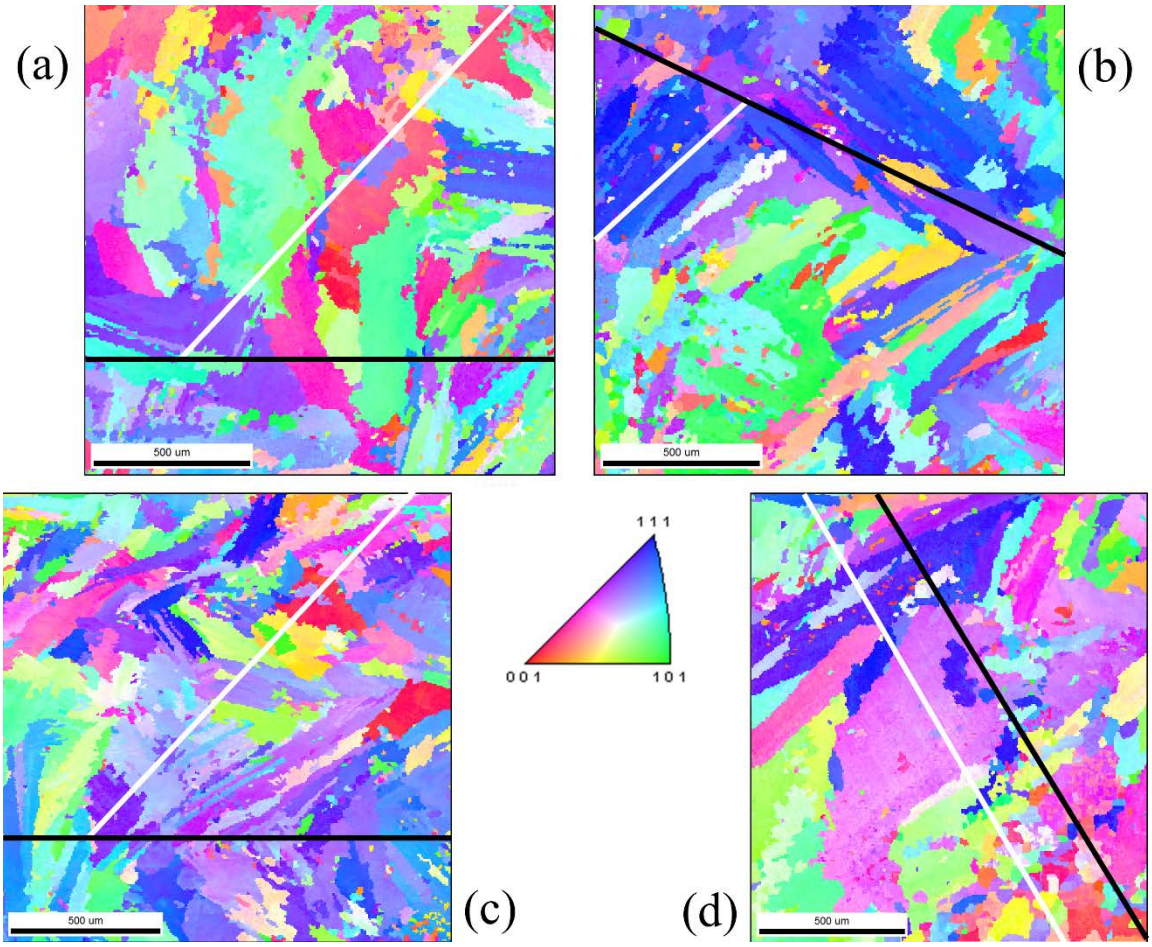

Figure 21. EBSD inverse pole figured for samples A (a), B (b), C (c), and D (d), with accompanying orientation key and indications of approximate

location of hatching/contour interface (black line) and scan direction (white line).

The EBSD micrograph of sample B shows a possible distinction between hatching lines and the contour through orientation. The contour and a possible hatching line tend toward [111], while the next distinct hatching line tends toward [101]. The grains appear to have aligned parallel to the laser scan direction; however, this is not corroborated by any of the other samples. In all of the samples, there was some consistency in grain orientation across the boundary between the contour and hatching. This indicates that because of re-melting, the grains in the material that were melted last grew in the same orientation as the already-solidified material.

Based on the area fractions of the different grain sizes, the microstructure of the faces was primarily coarse-grained, with some finer grains distributed throughout the scan area. This means that the combination of processing parameters caused the growth of the grains to prevail over nucleation. Because heat could not be lost to the rest of the sample and to the substrate fast enough to give a high enough cooling rate for a nucleation-prevalent microstructure, the grains were given ample time for growth during the solidification period. The development of an elongated microstructure was encouraged by the presence of nucleation sites from previously-melted material around the melt pool.

The discovery of coarse grains is contrary to some literature on LENS printing reporting a fine microstructure as a result of rapid cooling[13]. However, Tian et al reported large, elongated grains created by LENS-printing of IN718[38]. It is expected that this discrepancy is due to manufacturing differences that led to differences in thermal history. Since the machine that was used in this study is one of the first of its kind (a small-scale LENS machine for research laboratories) the small chamber experiences fast, intense heating, which would lessen the

microstructural rapid cooling effects. Industrial machines have larger chambers which take longer to heat up to the same temperatures. In addition, a discrepancy between the printing parameters used in this experiment (e.g. laser power, scan speed, layer height, etc.) and those used in other experiments could have caused enough of a difference to preclude the fine-grained microstructure.

2.3.4 Discussion of EBSD of cross-section

The cross-section of the LENS-printed sample showed mostly large, elongated grains. This is consistent with that of direct manufacturing processes that partially re-melt previous layers[39]. Large columnar grains are grown in LENS printing because the extension of the melt pool into the layer below creates a nucleus for the cooling liquid on the existing layer. The already-solidified grain's orientation therefore extends into the new layer[39]. The EBSD scans support this, since many grains are large enough to extend through several layers. These grains experience columnar growth because there is a positive temperature gradient from the solidified material into the melt pool[40]. This columnar microstructure may be beneficial for turbine applications.

The distribution of the smaller grains amongst the columnar grains can be explained by the overbuild of the contour. Both scans were taken from an area that was at the interface between the contour and the hatching, where there was a bend in the layers because the hatching overlapped the contour. There are fine grains scattered amongst the columnar grains all within this area, especially towards the top, where the overbuild was greatest. The overbuild is a bend in the layer, which allows for several points of contact with the already-solidified material. This would hinder solely columnar growth and increase nucleation sites, increasing the potential for growth of smaller grains (Figure 22).

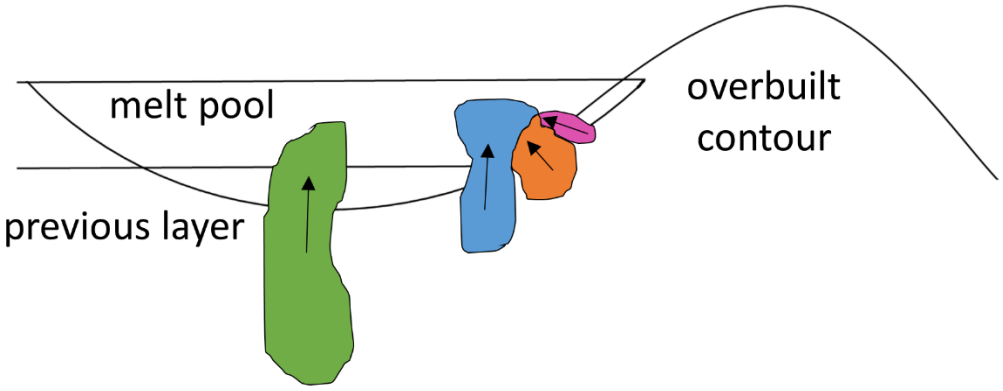

Figure 22. Schematic of potential grain growth due to contour overbuild.

2.4 VICKERS MICROHARDNESS: MECHANICAL PROPERTIES

2.4.1 Initial tests

Microhardness testing was performed in regions that spanned both hatching and contour, to detect any differences between the two. Initial testing used 300 gf and a 10 s dwell time on the faces of samples A, B, C, and D in a 5x4 grid. It is estimated that the final 2 rows of indents were within the contour in each sample. The calculated hardness values varied from 130 HV to 335 HV and were very scattered, with many outliers (Figure 23). Sample B had the lowest average hardness with 246 HV. Samples C and D had approximately the same average hardness, with 285 HV and 286 HV, respectively. Sample A had an average hardness of 270 HV. Samples A, C, and D had the largest range of data, with A and D having more outliers than C. Sample B had less scattered data, with less extreme outliers.

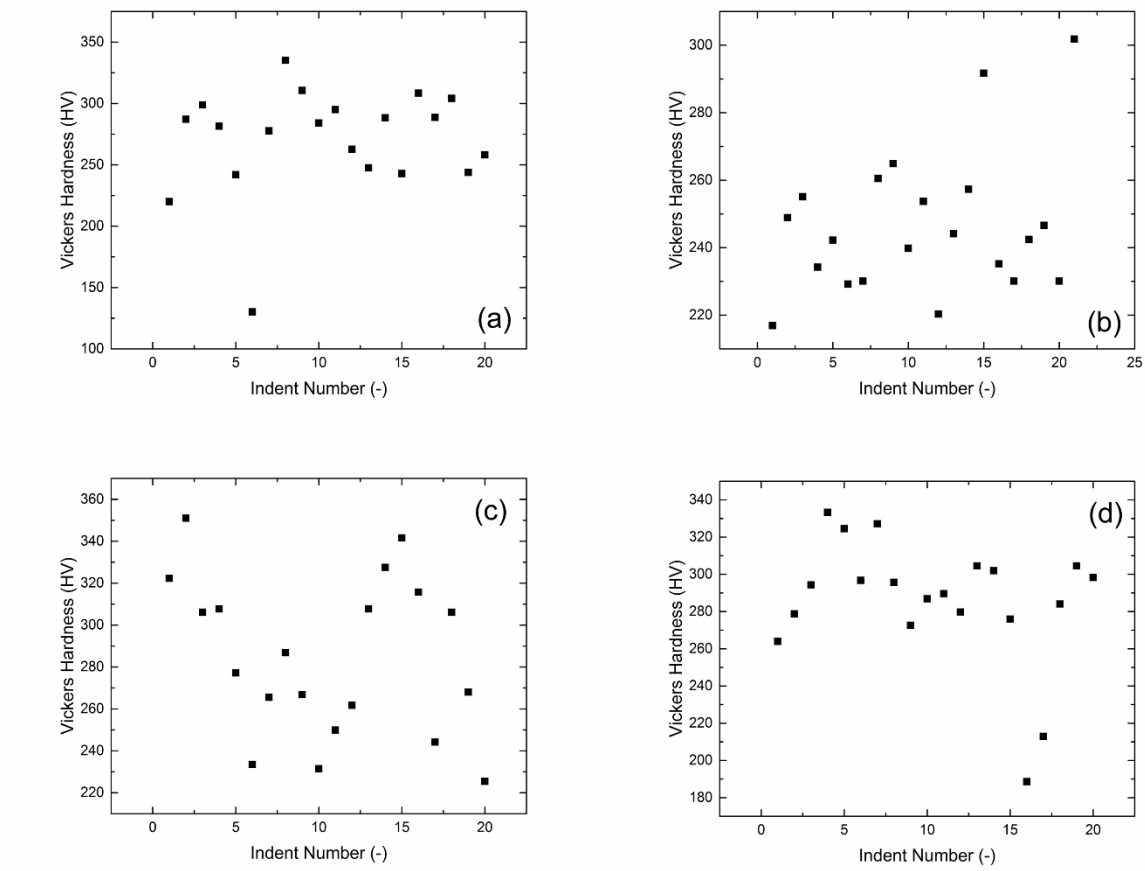

Figure 23. Vickers hardness values for 5x4 grid spanning hatching and contour. Test load of 300 gf and dwell time of 10 s were used. (a) sample A, (b) sample B, (c) sample C, (d) sample D

In order to collect more data and to attempt to decrease the standard deviation, another set of 5x4 grids were made, with an increased force of 500 gf. It is estimated that the final 2-3 rows of indents were within the contour out of the four in each sample. Overall, the standard deviation decreased and there were less extreme outliers (Figure 24). Sample B had an average hardness of 225 HV, and samples C and D had only slightly higher average hardness values of 232 HV and 233 HV. As in the first test, samples C and D had almost the same average hardness, but in the

second test, sample A had the highest hardness of 238 HV. Sample A also had a distinctly higher region for the first 13 indents and a distinctly lower region for the remaining 7 indents.

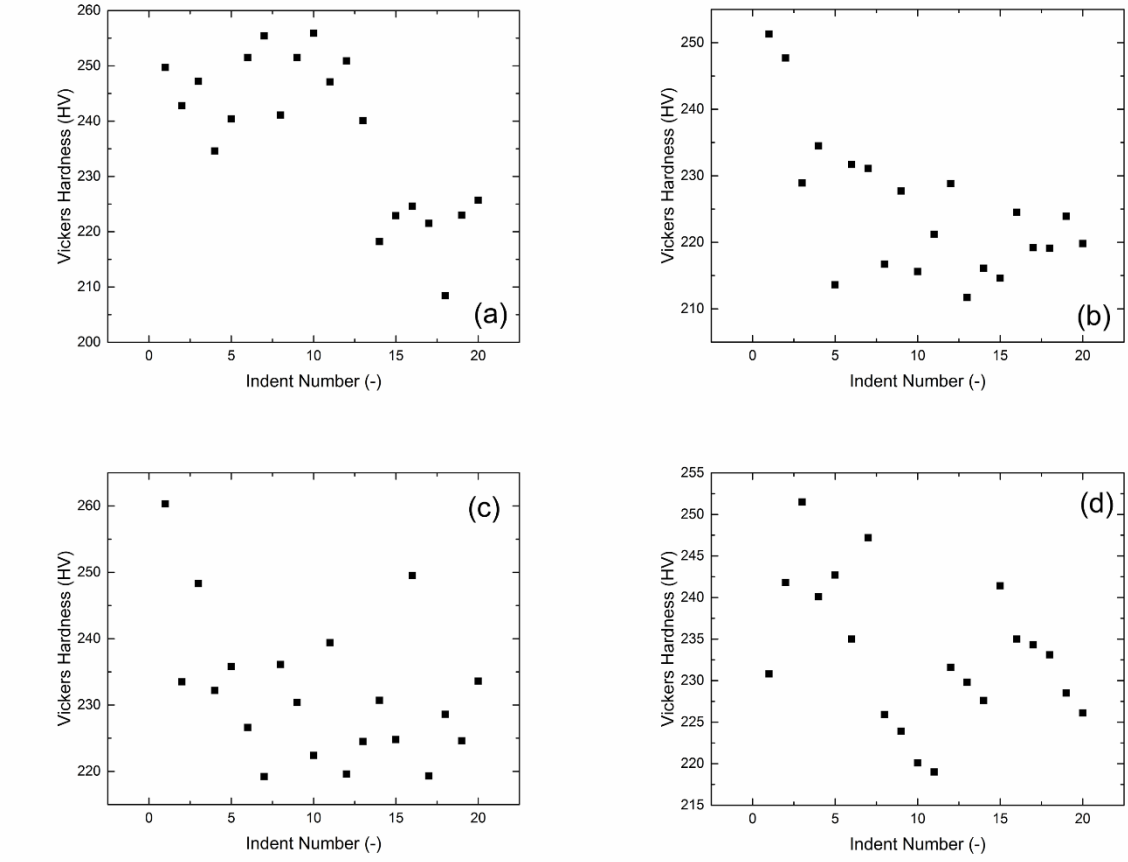

Figure 24. Hardness values for 5x4 grid of indents made with 500 gf load and a 10 s dwell time. (a) sample A, (b) sample B, (c) sample C, (d) sample D

2.4.2 Discussion of initial hardness tests

The first set of initial tests was done using a load of 300 gf. There were no distinct trends in any of the samples that would correlate to the location of the hatching and contour. When the samples were compared, sample B had the lowest average hardness with 246 HV (21.5 HRC), which is

closest to the reported values of hardness for a room-temperature hot-rolled round[41]. Samples C and D had the highest hardness of 285 HV and 286 HV (29.8 HRC and 30.0 HRC). These values are still lower than many of the reported hardness values for IN718, and they are in the range of values for a room-temperature hot-rolled bar[41]. Since a 300 gf load produced very scattered data, the load was increased in an attempt to increase precision and accuracy.

A 500 gf load increased the precision slightly, though the data was still somewhat scattered. Sample B still had the lowest hardness, sample A was the hardest based on this set of tests, and samples C and D still remained at almost the same hardness as each other. These consistent patterns and tendencies imply that there may be a difference in the hardness of the top layers of the samples: the printing parameters of sample B may have caused it to have a lower hardness, and the printing parameters of samples C and D may be similar enough to each other to have no effect on the hardness of the final samples. These hypotheses were evaluated through further testing.

In the second test, there was again no difference between the hatching and contour for samples B, C, and D; however, sample A showed a distinct difference in hardness between the hatching and the contour (Figure 25). Since the exposed surface was in an interlayer region, the pore density was lower in the hatching than in the contour, as discussed previously. This lower pore density left more material intact, and may have resulted in a higher average hardness. In the contour of sample A, where there were an increased number of densely-packed pores, the average hardness was lower by approximately 10%.

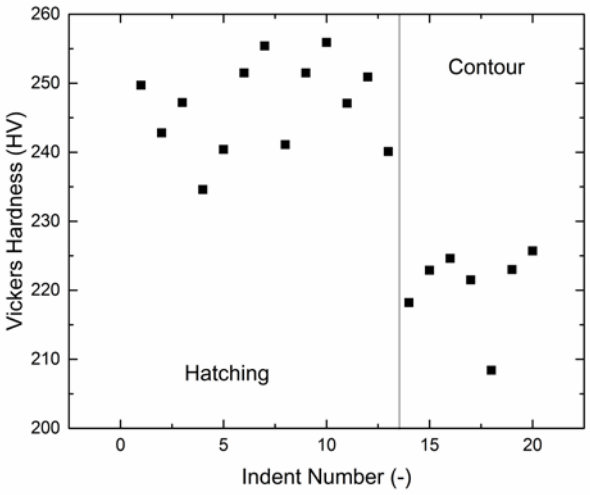

Figure 25. Distinction of the hatching and contour hardness values for the second set of hardness tests, with 500 gf load and 10 s dwell time.

2.4.3 Subsequent hardness testing

Since data from the initial tests was insufficient to confirm any hypotheses about differences in hardness between or within samples, subsequent testing was performed. First, a 5x6 grid of indents was made on each sample in a manner that spanned both the hatching and contour, with the final 2-3 rows in the contour. Then, hardness maps of the top and center slices of sample A were created. These maps sampled a quarter of the sample face, in order to infer the behavior of the remaining symmetrical ¾ of the samples (Figure 9**Error! Reference source not found.**).

2.4.3.1 Average hardness by row

Plotted averages of each row for each sample are shown in Figure 26. The first rows are in the hatching, and the higher number rows progressed into the contour. Sample A had a slight increasing trend with increasing row number, from 221 HV to 241 HV. Sample B decreased in

hardness from 237 HV in row 1 to 218 HV in row 5, and increased again to 231 HV in row 6. Sample C had a similar trend, decreasing from 238 HV in row 1 to 226 HV in row 5, then increasing to 232 HV in row 6. Sample D had consistently higher hardness values than the other samples, but did not have a distinct trend. Sample D started at 254 HV for row 1, decreased to 244 HV by row 3, increased to 252 HV in row 4, decreased to 240 HV in row 5, and increased again in row 6 to 249 HV.

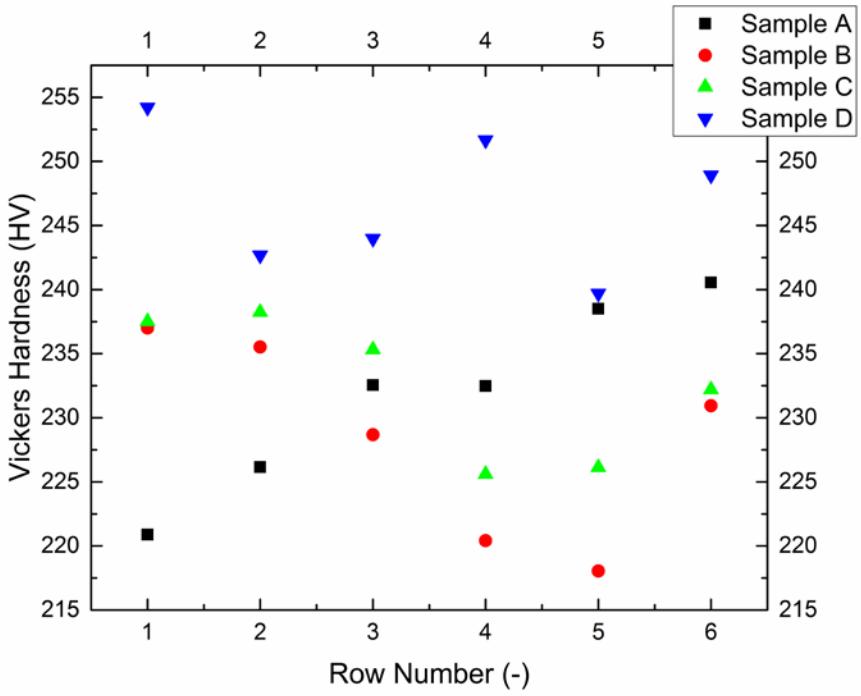

Figure 26. Average hardness per row for initial testing of samples A, B, C, and D.

An average of overall hardness for each sample is shown in Table 4. Sample D had a higher hardness value than samples A, B, and C with 247 HV. Sample B had the lowest hardness of 228 HV. Samples A and C both had an average of 232 HV.

Table 4. Average initial Vickers microhardness values for samples A, B, C, and D.

Sample	Hardness (HV)
A	232
B	228
C	232
D	247

2.4.4 Discussion of subsequent hardness testing

Though it appeared from the initial tests that there may be a difference in the hardness values in the contour and the hatching, there is no evidence to support this in the subsequent testing. There was no sharp decrease such as that seen in sample A from the initial tests (Figure 25), nor was there any consistent trend between the samples.

Consistent with the initial tests, sample B had a lower hardness; though by much more of an insignificant margin. Only 4 HV difference from a 5x6 grid of indents is not enough to conclude that the bulk hardness is lower than the other samples. Instead of samples C and D having almost the same hardness, samples A and C had similar hardness averages. As with the first set of tests, sample D had the highest hardness.

2.4.5 Hardness mapping

To improve the hardness measurements and to better understand the hardness distribution and local effects, the hardness was mapped on slices, faces, and cross-sections on sample A in order to determine if there was a distinct hardness distribution pattern.

2.4.5.1 Hardness mapping on slices

Sample A was cut into three slices: bottom, center, and top. These slices represented three different areas of thermal history.

The center slice was in the fourth or fifth layer, and had an average hardness of 263 HV. There was a distinct pattern to the hardness distribution: harder within the hatching, and less hard within the contour (Figure 27). The difference in the average hardness of the contour region and hatching region was approximately 20 HV. The highest hardness of 368 HV occurred at the top right corner of the testing area. The bottom left corner, corresponding with the corner of the sample, had the lowest hardness values, with the lowest being 213 HV.

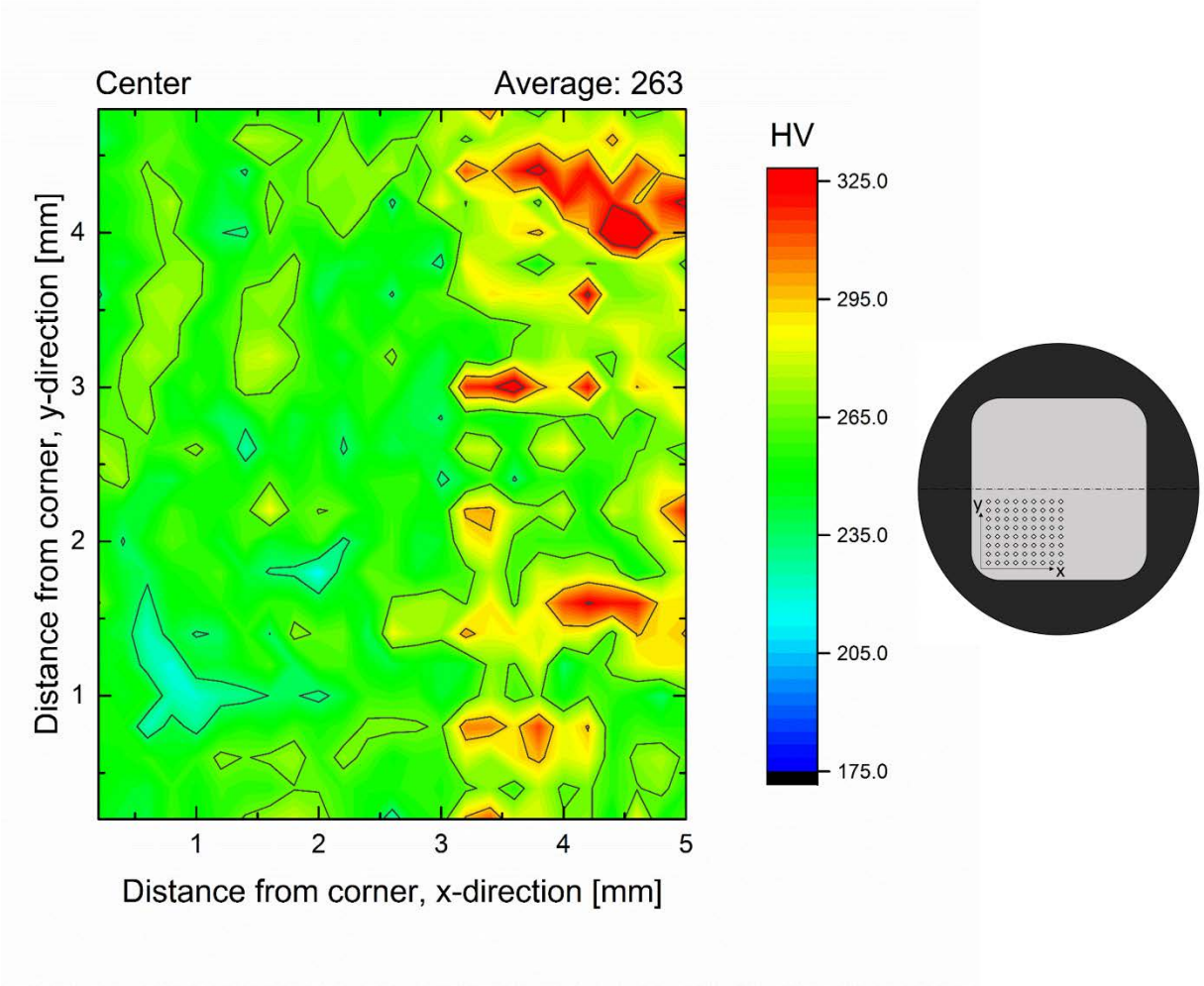

Figure 27. Contour map of hardness values in center slice of sample A.

The top slice was in the eighth or ninth layer, since the tenth layer had been removed with the initial polishing. Significantly lower than that of the center, the average hardness of the top slice was 228 HV. Similar to the center slice, the top showed a pattern to the hardness values corresponding to the contour or hatching: the hatching is harder than the contour. However, this difference is less consistent. The difference between the averages of the approximate contour and hatching areas is closer to 10 HV than the 20 HV of the center. There is also an area within the contour, in the bottom left corner, that matched the hardness values of the hatching (Figure 28).

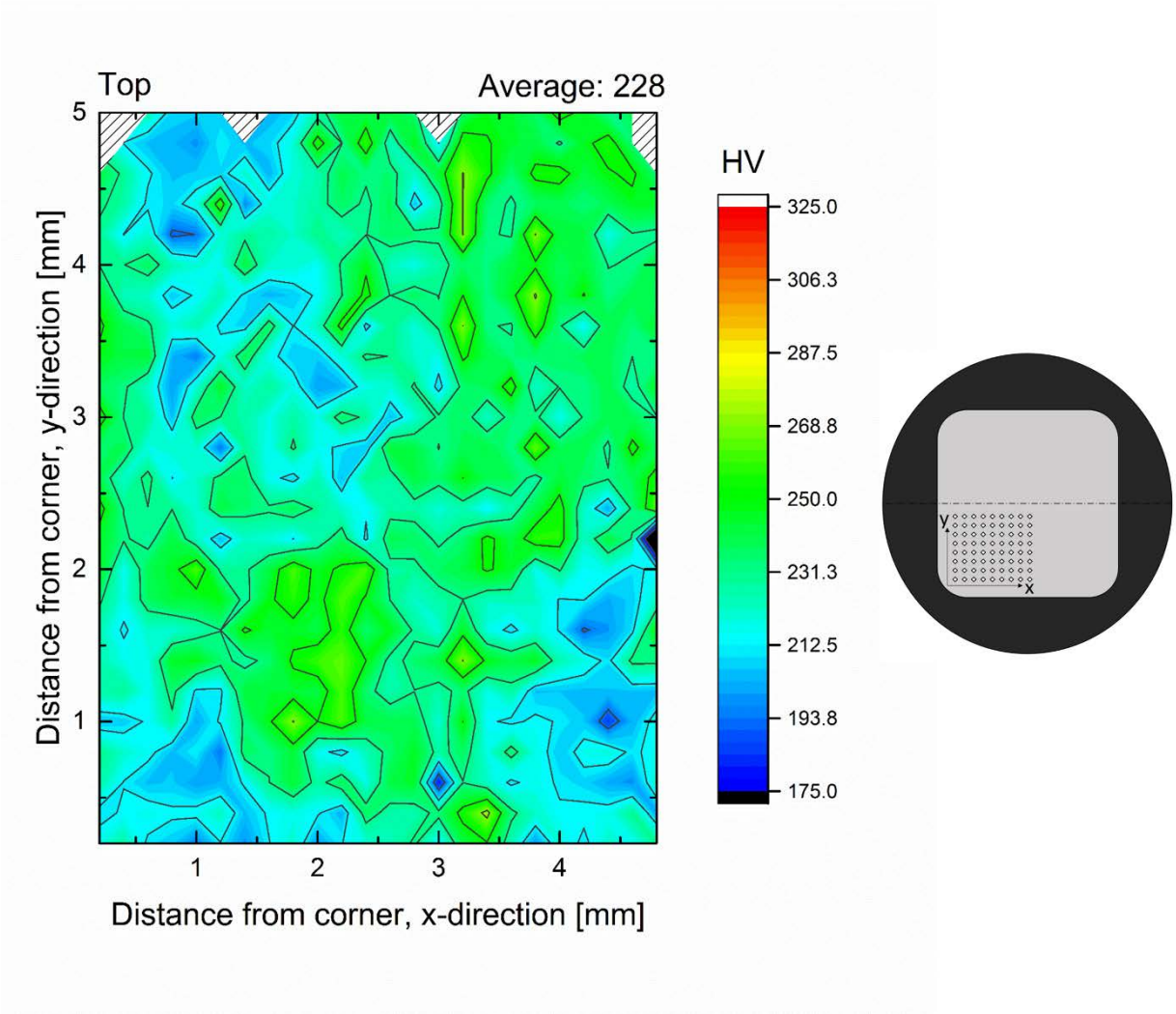

Figure 28. Contour map of hardness values in the top slice of sample A.

2.4.5.2 Hardness mapping on cross-section

Sample 1 was cut in half perpendicular to the substrate, and the cross-section was examined by creating a map of hardness values from the contour of the left side into the hatching (Figure 10). The data is shown in a contour map in Figure 29. The average of the hardness within the sample was 282 HV. The average hardness within the contour was 274 HV, and the average hardness within the hatching was slightly higher, at 290 HV. Overall, the contour was consistently

lower in hardness than the hatching, and the top overbuilt region of the contour had the lowest average hardness of approximately 259 HV.

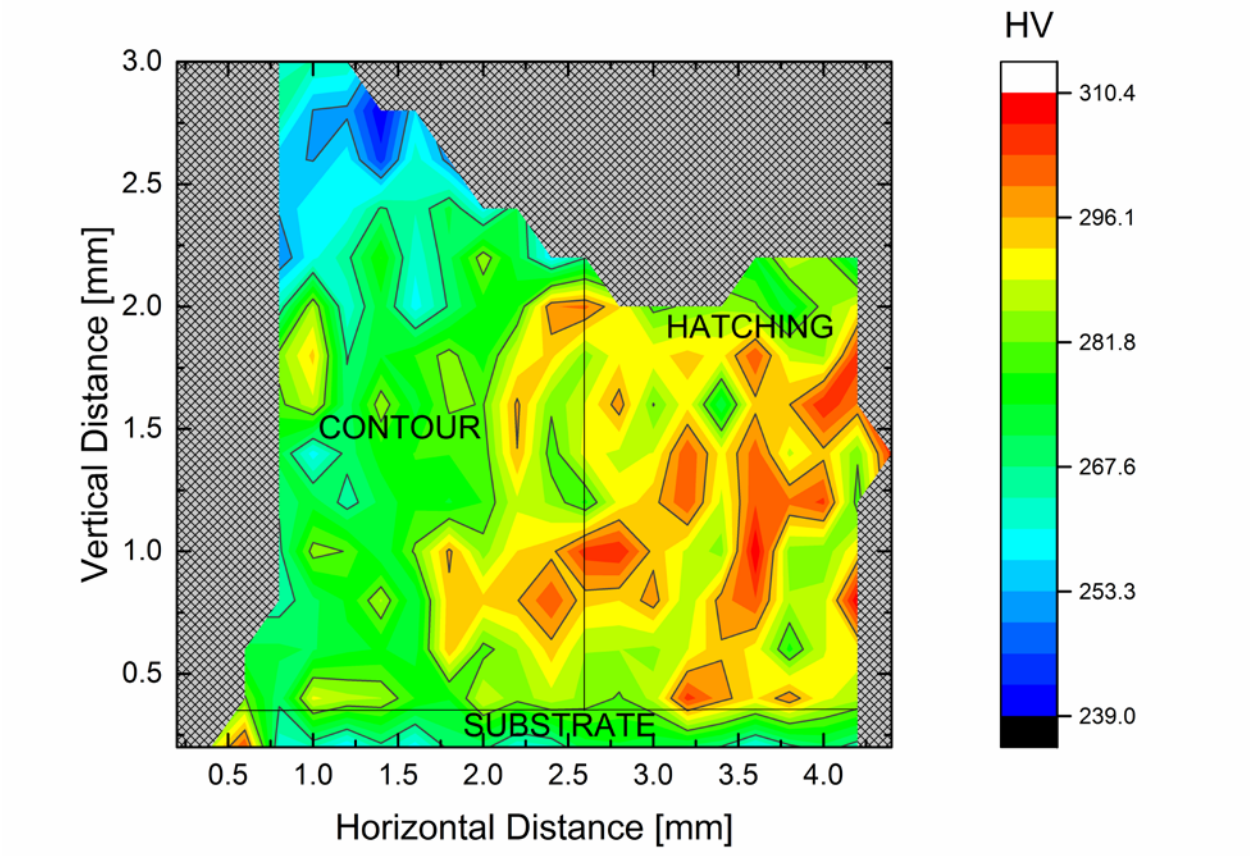

Figure 29. Hardness mapping for cross-section of sample 1.

2.4.6 Discussion of hardness mapping

Both the top and center slices indicated that there was a difference between the hardness of the contour and that of the hatching. This supports the results from the initial tests (section 2.4.2), though not the subsequent tests (section 2.4.4). It is possible that the subsequent tests were performed in an area which happened to show less difference in hardness between the two regions,

such as the bottom left corner and the hatching in Figure 28 (the top slice). The mapping presents more reliable results since the testing area was not arbitrarily selected. As has been discussed, the properties of a material are known to be anisotropic throughout a LENS-printed part, and this anisotropy is apparent here, both through the inconsistency of the small-grid hardness tests and through pattern formation in the results of the hardness mapping.

The cause of the difference in hardness could be a result of several factors: the pores discussed in section 2.4.2, the formation of different-sized grains within the contour, or the existence of different phases. It is not likely to be only an effect of the pores, since the samples used for mapping were not confirmed to be both polished to an interlayer surface; in addition, the dark field optical microscopy of the cross-section did not show a clear difference in pore distribution between the hatching and the contour. The formation of different-sized grains within the contour is possible due to different thermal history, but the EBSD results in section 2.3 show no indication that this is a significant consideration either for the sample face or for the cross-section.

The existence of a different phase distribution is possible. The matrix of IN718 is γ-phase, and the primary strengthening phase is γ″. Though γ″ is nano-sized, the particles can conglomerate and make an area rich in γ″. This effect, and the particles' presence in Nb- and Mo-rich areas was explored by Tian et al[38]. In section 2.2.2.2, the macro-segregation in the face of the samples was discussed, and it was concluded that solidification caused Nb and Mo to be swept to the edges of dendrites as well as the edge of melt pools. With an increased number of overlapping melt pools in the contour, these elements would get redistributed more frequently and in a more scattered manner, not allowing for the formation of a significant amount of γ″ in any one region. In the hatching however, Nb and Mo are swept systematically to the parallel edges of the melt pool as

the laser scans back and forth. This alignment of melt pool edges could allow for the formation of more conglomerated γ″ particles, which would result in a higher average hardness value in the hatching.

3.0 FUTURE WORK

When beginning this work, the ASM Handbook was consulted for grinding and polishing methods, and the information for nickel was used[42]. It was discovered after having begun the sample preparation that it produces better results to use the information for heat-resistant alloys instead. For consistency, the method was not changed for the duration of this study; however, future work will involve using surface preparation for heat-resistant alloys and comparing the results to those presented in this study to obtain more results and isolate any effects resulting from the metallographic preparation methods used. With the change of the preparation method, more EBSD results will be obtained in order to further examine the texture and grain size throughout the samples, both parallel and perpendicular to the substrate. XRD may also be used to characterize phase distribution. Once the characterization is complete and linked to potential processing factors, the printing process will be systematically changed in order to reverse engineer the microstructure of the LENS-printed material.

Porosity will be analyzed further by doing additional powder and sample characterization. Powders will be mounted in epoxy and ground to expose the center of some particles, which will be examined for internal porosity and trapped air. Samples will be examined using computer tomography to more accurately analyze pore shape, size, and distribution.

The methods and materials will also be expanded upon. Once the current method and material are understood, the project will be expanded to involve powder bed binder jet printing and IN625. Effects of variables such as powder size distribution, sintering time and temperature, and heat treatment methods will be evaluated. Effects of powder production method on both the powder bed binder jet printing and LENS printing will also be evaluated.

4.0 CONCLUSION

This study has explored the microstructural and mechanical properties of a nickel-based superalloy that has been additively manufactured. The material and process in focus were IN718 and Laser Engineered Net Shaping, respectively. Results from optical microscopy, scanning electron microscopy, energy-dispersive X-ray spectrometry, electron backscatter diffraction, and Vickers microhardness were analyzed.

1. The comparison between the polished and re-polished samples in conjunction with cross-sectional images showed that the pore distribution is likely associated with melt pool edges. The placement and interaction of these melt pool edges caused the intralayer hatching to be traced out by the pores, and the interlayer hatching as well as the contour to have densely-packed, randomly-distributed pores.

2. Elemental analysis showed that there was micro-segregation as well as macro-segregation present in the samples. The micro-segregation was caused by dendritic solidification, and resulted in a Fe-rich core, a slightly Nb-rich interdendritic region, and some very Nb-rich spots. Macro-segregation resulted in a Mo- and Nb-rich region at the edge of the last-melted area, which defined the boundary between the hatching and contour as well as between scan lines.

3. Grain size and distribution examination of the face revealed coarse, elongated grains that did not vary significantly between hatching and contour. Therefore, grains of a certain orientation continue from one region to another due to re-melting. Grain size and distribution examination of

the cross-section also showed coarse, elongated grains that did not vary significantly between hatching and contour. These elongated, columnar grains indicate that the solidified material in the previous layer serves as a nucleation site for the melt pool. Also, the bend in solidified material due to the overbuild of the contour may allow for more nucleation sites, resulting in more, smaller grains at this bend.

4. Initial and subsequent hardness testing with small grids of indents revealed no recognizable, consistent trend in hardness data, either in individual samples or between samples. Hardness mapping revealed a difference in the average hardness of the contour and the hatching. Locally, there was sometimes a great deal of variation, which highlights the shortcomings of small grid tests of arbitrary areas. The two slices that were tested on the face (top and center) both showed the hatching/contour variation, which may be a result of increased γ'' formation instigated by the macro-segregation of Nb and Mo.

APPENDIX A

ABBREVIATIONS

AM	additive manufacturing
BCT	body-centered tetragonal
BEC	backscatter electron composition (image)
CAD	computer-aided design
DOM	digital optical microscope
EBSD	electron backscatter diffraction
EDS	energy-dispersive X-ray spectroscopy
FCC	face-centered cubic
HAZ	heat-affected zone
IN718	Inconel alloy 718
LENS	Laser Engineered Net Shaping
PM	powder metallurgy
PREP	plasma rotating electrode process
SEM	scanning electron microscope

BIBLIOGRAPHY

1. Mellor, S., Hao, L. & Zhang, D. Additive manufacturing: A framework for implementation. *Int. J. Prod. Econ.* **149,** 194–201 (2014).
2. Holmström, J., Partanen, J., Tuomi, J. & Walter, M. Rapid manufacturing in the spare parts supply chain: Alternative approaches to capacity deployment. *J. Manuf. Technol. Manag.* **21,** 687–697 (2010).
3. Frazier, W. E. Metal additive manufacturing: A review. *J. Mater. Eng. Perform.* **23,** 1917–1928 (2014).
4. Gebhardt, A. Glossary: Terms and Abbreviations. *Underst. Addit. Manuf.* 151–164 (2011). doi:http://dx.doi.org/10.3139/9783446431621.bm
5. ASTM International. F 2792-12a - Standard Terminology for Additive Manufacturing Technologies. 10–12 (2013). doi:10.1520/F2792-12A.2
6. Gibson, I., Rosen, D. W. & Stucker, B. *Additive Manufacturing Technologies*. *Springer Science + Business Media, LLC* (2010). doi:10.1007/978-1-4419-1120-9
7. Moroni, G., Syam, W. P. & Petr, S. Towards early estimation of part accuracy in additive manufacturing. **21,** 300–305 (2014).
8. Gebhardt, A. in *Understanding Additive Manufacturing* 1–29 (Hanser Publishers, 2012).
9. Dudziak, A. *et al.* Accuracy of parts manufactured by rapid prototyping technology. (2010).
10. Gebhardt, A. in *Understanding Additive Manufacturing* 31–63 (Hanser Publishers, 2011). doi:http://dx.doi.org/10.3139/9783446431621.002
11. Manvatkar, V. D., Gokhale, a. a., Jagan Reddy, G., Venkataramana, a. & De, a. Estimation of melt pool dimensions, thermal cycle, and hardness distribution in the laser-engineered

net shaping process of austenitic stainless steel. *Metall. Mater. Trans. A Phys. Metall. Mater. Sci.* **42,** 4080–4087 (2011).

12. Palčič, I., Balažic, M., Milfelner, M. & Buchmeister, B. Potential of Laser Engineered Net Shaping (LENS) Technology. *Mater. Manuf. Process.* **24,** 750–753 (2009).
13. Grylls, R. Laser Engineered Net Shapes.pdf. 45–46 (2003).
14. Keicher, D. M. & Smugeresky, J. E. The laser forming of metallic components using particulate materials. *Jom* **49,** 51–54 (1997).
15. Liu, D. *et al.* Laser Engineered Net Shape (LENS) Technology for the Repair of Ni-Base Superalloy Turbine Components. *Metall. Mater. Trans. A* **45,** 4454–4469 (2014).
16. Cooper, K. P. Building components by laser-additive processing. *Jom* **53,** 29–29 (2001).
17. Liu, W. & Dupont, J. N. In-situ reactive processing of nickel aluminides by laser-engineered net shaping. *Metall. Mater. Trans. A* **34,** 2633–2641 (2003).
18. Tobar, M., Amado, J., Lamas, J. & Yáñez, a. Effect of Processing Parameters in Manufacturing of 3D parts Through Laser Direct Metal Deposition. 4–7
19. Donachie, M. J. & Donachie, S. J. *Superalloys: a technical guide*. (ASM International, 2002).
20. Reed, R. C. *The superalloys: fundamentals and applications*. (Cambridge University Press, 2006).
21. Smith, G. D. & Patel, S. J. The Role of Niobium in Wrought Precipitation-Hardened Nickel-Base Alloys. *Superalloys 718, 625, 706 Var. Deriv.* 135–154 (2005). doi:10.7449/2005/Superalloys_2005_135_154

22. Kulawik, K., Buffat, P. a., Kruk, a., Wusatowska-Sarnek, a. M. & Czyrska-Filemonowicz, a. Imaging and characterization of γ′ and γ″ nanoparticles in Inconel 718 by EDX elemental mapping and FIB–SEM tomography. *Mater. Charact.* **100,** 74–80 (2015).

23. Wang, L., Felicelli, S., Gooroochurn, Y., Wang, P. T. & Horstemeyer, M. F. Optimization of the LENS?? process for steady molten pool size. *Mater. Sci. Eng. A* **474,** 148–156 (2008).

24. Zhang, Y., Li, Z., Nie, P. & Wu, Y. Effect of cooling rate on the microstructure of laser-remelted INCONEL 718 coating. *Metall. Mater. Trans. A Phys. Metall. Mater. Sci.* **44,** 5513–5521 (2013).

25. Zhao, X., Chen, J., Lin, X. & Huang, W. Study on microstructure and mechanical properties of laser rapid forming Inconel 718. *Mater. Sci. Eng. A* **478,** 119–124 (2008).

26. Porter, D. A., Easterling, K. E. & Sherif, Y. *Phase Transformations in Metals and Alloys*. *Annual Review of Materials Science* **3,** (2009).

27. Hofmeister, W. & Griffith, M. Solidification in direct metal deposition by LENS processing. *JOM* **53,** 30–34 (2001).

28. Yin, H. & Felicelli, S. D. Dendrite growth simulation during solidification in the LENS process. *Acta Mater.* **58,** 1455–1465 (2010).

29. Qi, H., Azer, M. & Ritter, A. Studies of Standard Heat Treatment Effects on Microstructure and Mechanical Properties of Laser Net Shape Manufactured INCONEL 718. *Metall. Mater. Trans. A* **40,** 2410–2422 (2009).

30. Zheng, B., Zhou, Y., Smugeresky, J. E., Schoenung, J. M. & Lavernia, E. J. Thermal behavior and microstructure evolution during laser deposition with laser-engineered net shaping: Part II. Experimental investigation and discussion. *Metall. Mater. Trans. A Phys. Metall. Mater. Sci.* **39,** 2237–2245 (2008).

31. Peter J. Goodhew, F. J. Humphreys, R. B. *Electron microscopy and analysis*. *Electron Microscopy and analysis* (2001).

32. Garratt-Reed, a J. & Bell, D. C. Energy-Dispersive X-Ray Analysis in the Electron Microscope. *Microscopy* **49,** 1–13 (2003).

33. Stojakovic, D. Electron backscatter diffraction in materials characterization. *Process. Appl. Ceram.* **6,** 1–13 (2012).

34. Cullity, B. D. & Stock, S. R. *Elements of x-ray diffraction*. (Prentice Hall, 2001).

35. Astm. ASTM E 407 Standard Practice for Microetching Metals and Alloys 1. 1–21 (2005). doi:10.1520/E0407-07.2

36. *Hardness testing: principles and applications*. (ASM International, 2011).

37. Dieter, G. & Bacon, D. Mechanical Metallurgy. *McGrawHill Shoppenhangers Road Maidenhead Berkshire SL2 2QL UK 1988* (1988).

38. Tian, Y. *et al.* Rationalization of Microstructure Heterogeneity in INCONEL 718 Builds Made by the Direct Laser Additive Manufacturing Process. (2014). doi:10.1007/s11661-014-2370-6

39. Vilaro, T., Colin, C. & Bartout, J. D. As-fabricated and heat-treated microstructures of the Ti-6Al-4V alloy processed by selective laser melting. *Metall. Mater. Trans. A Phys. Metall. Mater. Sci.* **42,** 3190–3199 (2011).

40. Kurz, W., Bezençon, C. & Gäumann, M. Columnar to equiaxed transition in solidification processing. *Sci. Technol. Adv. Mater.* **2,** 185–191 (2001).

41. INCONEL alloy 718. 1–27 (2007).

42. ASM-Standard. Metallography and Microstructures of Nonferrous Alloys. *ASM Handb.* **9,** 711–751 (2004).